Matthias Leitner, BSc

Synthesis and Positron Annihilation Lifetime Spectroscopy of Nanoporous Platinum

MASTER THESIS

For obtaining the academic degree
Diplom-Ingenieur

Master Programme of
Technical Physics

Graz University of Technology

Supervisor:

Assoc. Prof. Dipl.-Phys. Dr.rer.nat. Wolfgang Sprengel

Institute of Materials Physics

Graz, July 2015

EIDESSTATTLICHE ERKLÄRUNG

AFFIDAVIT

Ich erkläre an Eides statt, dass ich die vorliegende Arbeit selbstständig verfasst, andere als die angegebenen Quellen/Hilfsmittel nicht benutzt, und die den benutzten Quellen wörtlich und inhaltlich entnommenen Stellen als solche kenntlich gemacht habe. Das in TUGRAZonline hochgeladene Textdokument ist mit der vorliegenden Masterarbeit/Diplomarbeit/Dissertation identisch.

I declare that I have authored this thesis independently, that I have not used other than the declared sources/resources, and that I have explicitly indicated all material which has been quoted either literally or by content from the sources used. The text document uploaded to TUGRAZonline is identical to the present master's thesis/diploma thesis/doctoral dissertation.

_____ _____

Datum / Date Unterschrift / Signature

Abstract

Platinum exhibits a negative work function for positrons, such that a positron thermalized near the surface can be emitted from the crystal. Such a positron can pick up an electron and form positronium at the surface. Therefore, a platinum sample with a high surface-to-volume ratio should be an ideal candidate for a positronium source. Nanoporous platinum, exhibiting a highly interconnected porous structure and therefore a high specific surface area, can be fabricated by electrochemical dealloying, i.e., selective etching of platinum alloys.

The aim of this work was to prepare different types of nanoporous platinum by dealloying of a $Cu_{75}Pt_{25}$ alloy and by compaction of nanocrystalline platinum powder for comparison. The ability to form positronium and the behavior of the ortho-Ps lifetime was analyzed by positron lifetime spectroscopy after different sample treatments and under various measurement conditions. A long lifetime component corresponding to positronium annihilation was observed, however the intensity was less than one percent. The vast majority of annihilation events results from positrons annihilating from surface defects.

Kurzfassung

Aufgrund der negativen Positronen-Austrittsarbeit von Platin ergibt sich für Positronen, welche nahe der Oberfläche thermalisiert werden, die Möglichkeit aus dem Kristall emittiert zu werden. An der Oberfläche kann das Positron ein Elektron einfangen und Positronium bilden. Platinproben mit hohem Oberflächen-zu-Volumen-Verhältnis sollten sich daher als Positronium Quellen eignen. Nanoporöses Platin, welches eine stark ineinandergreifende, poröse Struktur aufweist, kann durch elektrochemisches Dealloying, d.h. durch selektives Ätzen, aus Platinlegierungen hergestellt werden.

Das Ziel dieser Arbeit war es, nanoporöses Platin durch Dealloying einer $Cu_{75}Pt_{25}$ Legierung sowie durch Kompaktion von nanokristallinem Platinpulver als Vergleichsprobe herzustellen. Mithilfe der Positronen Lebensdauer Spektroskopie wurde die Positroniumbildung sowie das Verhalten der ortho-Ps Lebensdauer nach unterschiedlichen Probenbehandlungen und unter verschiedenen Messbedingungen analysiert. Es konnte eine lange Lebensdauerkomponente beobachtet werden, welche der Positroniumzerstrahlung zugeordnet werden kann. Die zugehörige Intensität ist jedoch geringer als ein Prozent. Der Großteil der Zerstrahlungsereignisse resultiert von Positronen-Zerstrahlung in Oberflächendefekten.

Contents

1 Introduction **1**

2 Fundamentals **3**

2.1 Positron Annihilation in Solids 3
2.1.1 Positron Source ^{22}Na 5
2.1.2 Positron Implantation Profile 6

2.2 Positronium (Ps) 8
2.2.1 Negative Positron and Positronium Work Function 9
2.2.2 Ps Formation at Metal Surfaces using Foil Sources 10

2.3 Positron Annihilation Lifetime Spectroscopy 11
2.3.1 The Lifetime Analysis Software PALS*fit* 13
2.3.2 The Mean Positron Lifetime τ_m 14

3 Synthesis and Characterization of Nanoporous Platinum **15**

3.1 Fundamentals of Electrochemical Dealloying 15

3.2 Experimental Methods 17
3.2.1 Chrono Amperometry (CA) - Dealloying 18
3.2.2 Cyclic Voltammetry (CV) 19
3.2.3 Different Experimental Approaches for Dealloying of $Cu_{75}Pt_{25}$ 21
3.2.4 Synthesis of Nanoporous Pt via Dealloying of $Cu_{75}Pt_{25}$ 23
3.2.5 Synthesis of Nanoporous Pt via Powder Compaction. 25
3.2.6 Sample Treatment 25

3.3 Results - Dealloying Curves and Accumulated Charge 27

3.4 Results - Cyclic Voltammetry and Specific Surface Determination 32

4 Fast-Fast Positron Lifetime Spectrometer 35

4.1 Functional Principle 35

4.2 Mounting in Sandwich Geometry 37

4.3 Measurements under Vacuum Condition 38

4.4 Time Scale of the Spectrometer 39

4.5 Resolution Function of the Spectrometer 40

5 Positron Lifetime Results 43

5.1 Ps Formation in Teflon 45

5.2 Positron Lifetime Measurements with np-Pt180 46

5.3 Positron Lifetime Measurements with np-Pt300 49

5.4 Positron Lifetime Measurements with Pt-Pellets 52

6 Discussion 57

6.1 Conclusions derived from Stages I - III 58

6.1.1 Stage I: As-prepared → After oxide reduction 58

6.1.2 Stage II: After oxide reduction (air) → After oxide reduction (vacuum) 59

6.1.3 Stage III: After oxide reduction (vacuum) → After annealing (vacuum) 60

6.2 Detailed Positron Lifetime Analysis 60

6.2.1 Pt-Pellets 60

6.2.2 np-Pt 62

7 Conclusion 65

Bibliography 67

A Appendix 73

Programs for Data Pre-processing 73

Acknowledgment 77

CHAPTER 1

Introduction

Positrons and positronium are versatile nuclear probes for the study of materials. While positrons are mostly used to study the bulk properties of materials on an atomistic scale, the quasi-stable bound state between an electron and a positron, the so-called positronium atom (Ps), can be used to probe surfaces or pores of materials. The following work will focus on the probability of positronium formation in nanoporous platinum and its possible application.

Different scenarios for Ps formation are possible but all are related to the surface of the metal. One important aspect to mention in this context is the positron work function. For metals exhibiting a negative e^+ work function, the positrons inside the bulk feel an expelling potential and gain energy upon leaving the metal [1]. Outside the last atomic layer, the positrons can then capture an electron and form Ps, while inside the metal the electron density is too high for Ps formation [2]. Various slow-positron-beam experiments have been conducted in the past to study the formation of Ps at single crystal metallic surfaces in vacuum [3–8].

At this point one question arises: what happens if positrons are injected into nanoporous materials with a negative positron work function? Obviously, then there is no need for slow positron beams in order to implant positrons close beneath the surface, which can be ejected and form Ps. Instead, conventional foil sources, generating a spectrum of positrons with different energies, can be used, since all positrons implanted into the material will eventually thermalize close to a surface due to the high specific surface area of the sample. Subsequently, the positrons might be emitted into a pore because of the negative positron

work function and form Ps.

There are two possible spin configurations the Ps atom can exist in. The singlet configuration $^1S_0$ where electron and positron exhibit anti-parallel spin, is called para-Positronium (p-Ps). It annihilates after a typical lifetime of 125 ps. The second possibility is the triplet configuration $^3S_1$ where the spins of the electron and the positron are aligned parallel. This configuration is called ortho-Positronium (o-Ps) and decays after a long vacuum lifetime of 142 ns [9].

However, this long o-Ps lifetime can be considerably shortened through the interaction with other molecules and atoms. This process where the positron does not annihilate with its bound electron but rather with a spin-antiparallel electron from the surrounding is called pick-off annihilation and can lead to lifetimes as short as 1 ns [10].

The effect of adsorbed gases on the pore walls of the nanoporous structure could then influence the o-Ps lifetime through pick-off quenching and might be useful for a sensor application.

To investigate this idea, a nanoporous, sponge-like Pt structure was fabricated. The choice of material was made because Pt exhibits a negative positron work function of $\Phi_+ = -1.8\,\mathrm{eV}$ [11] and it can be fabricated with a high specific surface area via dealloying of $Cu_{75}Pt_{25}$. In this dealloying process, the less noble component Cu is selectively dissolved. The result is a highly interconnected, porous Pt structure with ligament and pore sizes on the order of several nm [12].

Furthermore, no positron lifetime studies have been undertaken so far for nanoporous metals prepared by dealloying, except for nanoporous gold, which however exhibits a positive positron work function [13].

CHAPTER 2

Fundamentals

2.1 Positron Annihilation in Solids

Positron annihilation is a powerful method to non-destructively investigate matter by the use of the antiparticle of the electron, the positron e^+. The only difference to the electron is its positive elementary charge.

When a positron penetrates into a solid, it slows down to thermal energies in just a few ps due to inelastic collisions [14]. This process is called thermalization. The main energy-loss processes are core ionization [15] and excitation of conduction electrons (or electron hole pairs in semiconductors) [14]. Plasmon excitations [16] and phonon scattering at low energies [15] do also play a role during the slowing process. The mean implantation depth in solids is typically between 10 and 100 μm, depending on the source used and the density of the material [17] (see Section 2.1.2).

Once thermalized, the positron starts to diffuse. The mean positron diffusion length L_+ can be described by

$$L_+ = \sqrt{D_+ \tau_b}, \tag{2.1}$$

where τ_b is the positron lifetime in the defect-free bulk of the sample and D_+ is the positron diffusion coefficient [14,17]. In metals and semiconductors, D_+ shows values in the range of 1 to 3 $\mathrm{cm^2 s^{-1}}$ at 300 K [17]. For typical values of τ_b in the range of 100 to 200 ps, the mean diffusion length results in 100 to 200 nm [17].

The thermalized positrons will then either annihilate in the bulk material, or get trapped

into a defect, e.g., a vacancy because of the missing repelling potential of the positively charged core (compare trapping model in Section 2.3). The e^+ will predominantly annihilate into two collinearly emitted gamma rays, each carrying the rest energy of $m_0c^2 = 511\,\mathrm{keV}$. This is the inverse effect of the pair production.
In a homogenous electron gas, the annihilation rate λ, which is the inverse of the lifetime τ, is proportional to the electron density n

$$\lambda = \tau^{-1} = r_0^2 \pi c n, \tag{2.2}$$

where r_0 is the classical electron radius and c is the speed of light [17]. The corresponding experimental technique is called **P**ositron **A**nnihilation **L**ifetime **S**pectroscopy (PALS) which is described in Section 2.3.

Due to momentum conservation, the two gamma rays are only emitted collinearly if the e^-e^+ pair is at rest, resulting in two quanta of the energy 511 keV. However, because the electrons exhibit a non-zero momentum, there will be a slight deviation from collinearity on the order of several mrad in order to satisfy momentum conservation. The corresponding angle Θ can be described by

$$\Theta = \frac{p_\perp}{m_0 c}, \tag{2.3}$$

where $p_\perp$ is the contribution of the e^-e^+ momentum perpendicular to the annihilation radiation propagation direction, m_0 is the rest mass of the electron and c is the speed of light. Analysis of the measured angle Θ is done in so-called **A**ngular **C**orrelation of **A**nnihilation **R**adiation (ACAR) experiments.

Furthermore, the energies of the two quanta are Doppler shifted according to the formula

$$\Delta E = \frac{p_\parallel c}{2}, \tag{2.4}$$

where $p_\parallel$ is the momentum component parallel to the annihilation radiation propagation direction and c is the speed of light.

Since the positron is thermalized in the solid before annihilation, the momentum mostly originates from the e^-. Therefore, ACAR and Doppler broadening measurements reveal information about the electron momentum distribution.

Figure 2.1 sums up the basic principles behind the three experimental positron annihilation methods.

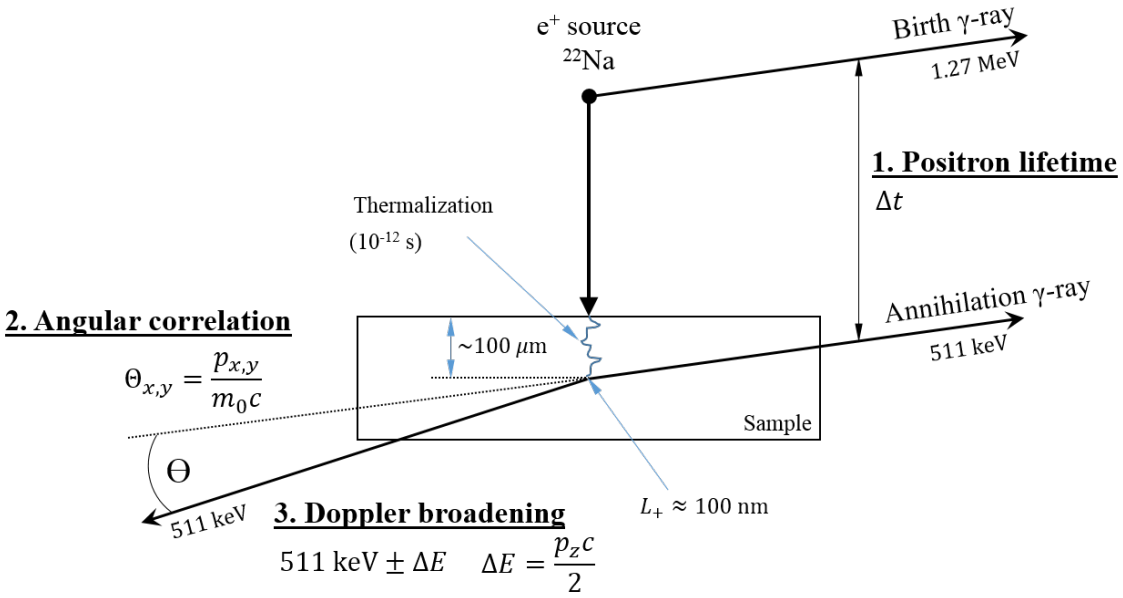

Figure 2.1: The positron is emitted from a ^{22}Na source and is thermalized in the sample. After diffusion it annihilates with an electron of the solid. (1) The time difference between the formation of the positron and the emission of annihilation radiation is measured in positron lifetime experiments. (2) The deviation from collinearity of the two quanta is measured in angular correlation of annihilation radiation measurements. (3) Doppler broadening describes an energy shift of $m_0c^2 \pm \Delta E$ for the annihilation radiation. Redrawn after reference [14].

2.1.1 Positron Source ^{22}Na

A very suitable radioactive source to be used in positron annihilation experiments in laboratories is ^{22}Na. This β^+-emitter has the advantage of a very high positron yield (90 %) and a rather long half-life of 2.6 years. Furthermore, ^{22}Na emits a 1275 keV γ-quantum just a few picoseconds after the emission of a positron (prompt γ-quantum) [9]. For positron lifetime experiments, this event is absolutely necessary because it marks the formation of the e^+ (start-quantum). Figure 2.2 depicts the decay scheme of ^{22}Na.
The primarily occurring process reads as

$$^{22}\mathrm{Na} \rightarrow {}^{22}\mathrm{Ne} + \mathrm{e}^+ + \nu_e + E.$$

The energy E that is emitted during the β^+ decay is shared among the emitted particles. Therefore, the spectrum of the positrons is continuous. It shows a transition energy at $E_{max} = 544\,\mathrm{keV}$ [9].

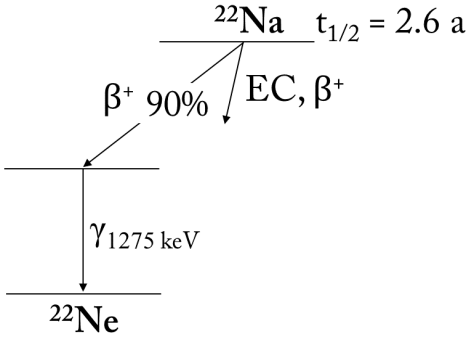

Figure 2.2: Decay scheme of ^{22}Na.

2.1.2 Positron Implantation Profile

Since preferably all positrons which are injected into the sample should entirely annihilate within this sample, it is important to know how the positron intensity $I(z)$, i.e., the number of positrons, decays with penetration depth. This decay can be described by an empirically found formula (Brandt and Paulin [18]).
According to this formula, the intensity of positrons shows an exponential decay with implantation depth z,

$$I(z) = I_0 \underbrace{\exp(-\alpha_+ z)}_{\overline{P}(z)}, \tag{2.5}$$

where $\overline{P}(z)$ is the positron implantation profile, i.e., the fraction of positrons reaching depth z [19]. The absorption coefficient α_+ can be described as a function of the mass density ρ of the irradiated solid and the maximum kinetic energy E_{max} of the positrons originating from the source

$$\alpha_+ \ [\mathrm{cm}^{-1}] \approx 17 \frac{\rho \ [\mathrm{g\ cm}^{-3}]}{E_{max}^{1.43} \ [\mathrm{MeV}]}. \tag{2.6}$$

Therefore, the number of positrons which will be thermalized in a depth smaller than z can be described by the stopping profile $S_p(z) = 1 - \overline{P}(z)$ [14]. Combining (2.5) and (2.6) yields

$$\overline{P}(z) = \exp\left(-\frac{17}{E_{max}^{1.43}} \cdot \rho z\right). \tag{2.7}$$

Figure 2.3 depicts the positron implantation profile for various elements and materials while in Figure 2.4, the e^+ implantation profile for positrons from a ^{22}Na source is shown as a function of ρz. Note that for this source, the quotient in the exponential is $\frac{17}{0.544^{1.43}} = 40.6\,\mathrm{cm^2/g}$. Thus for $\rho z = \frac{1}{40.6}\,\mathrm{g/cm^2} = 24.6\,\mathrm{mg/cm^2}$, the positron implantation profile decays to $1/e$ ($\approx 37\,\%$). The corresponding depth is called the mean penetration depth [14].

For $\rho z \approx 50\,\mathrm{mg/cm^2}$ the fraction decays to $1/e^2$ ($\approx 14\,\%$) et cetera. This is a useful rule of thumb for quick estimation of the necessary sample thickness of the investigated material.

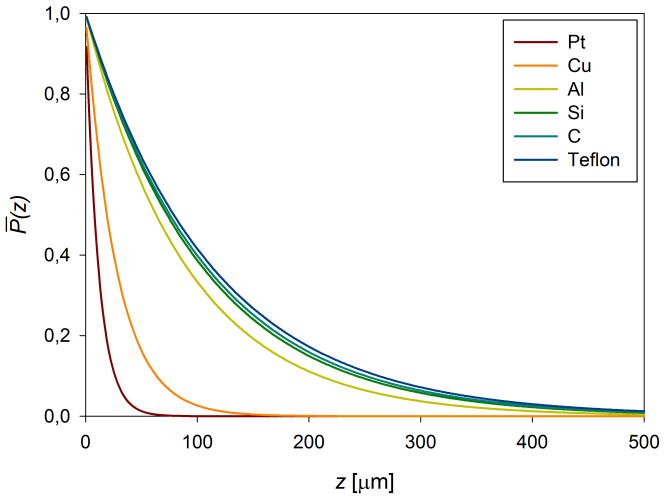

Figure 2.3: Implantation profile $\overline{P}(z)$ as a function of depth z for various elements and materials while using a ^{22}Na positron source.

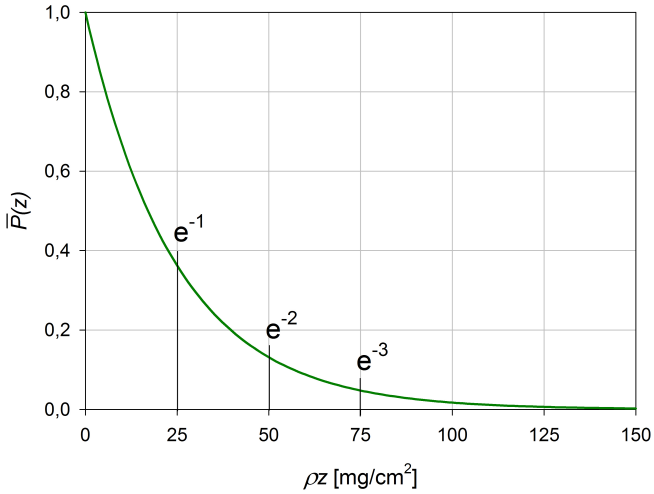

Figure 2.4: Positron implantation profile as a function of areal density ρz for positrons from a ^{22}Na source.

Solving (2.7) for the thickness z where the intensity decayed to the fraction $P \in [0, 1]$ of the initial positron intensity, yields

$$z(P, \rho)\ [\mu\mathrm{m}] = -\frac{246 \cdot \ln(P)}{\rho\ [\mathrm{g\ cm^{-3}}]}. \tag{2.8}$$

2.2 Positronium (Ps)

Positronium (Ps) is a quasi-stable hydrogen-like bound state between an electron and a positron [17].

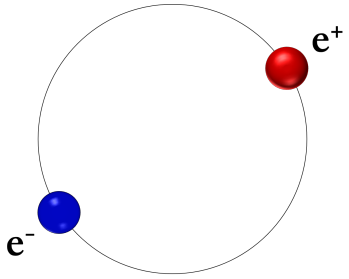

Figure 2.5: Schematical depiction of the Ps-atom.

There are two possible spin configurations. The spin-antiparallel Ps-atom (para-Positronium p-Ps, singlet state $^1S_0$) and the spin-parallel Ps-atom (ortho-Positronium o-Ps, triplet state $^3S_1$). Due to its total spin of $S_T = 1$, the ortho-Ps has a multiplicity of $2S_T + 1 = 3$, whereas for para-Ps, $2S_S + 1 = 1$ is true. This means that 75 % of the generated Ps-Atoms will exist in the triplet state [9].

Due to angular momentum conservation, the o-Ps can only decay into three quanta, which is a factor of 372 more unlikely than the two-gamma decay for p-Ps. This manifests itself in the very different vacuum lifetimes of o-Ps and p-Ps of $\tau_{o-Ps} = 142\,\text{ns}$ and $\tau_{p-Ps} = 125\,\text{ps}$, respectively [9]. However, the o-Ps can undergo various quenching mechanisms, that drastically reduce its lifetime.

Pick-off Annihilation

Pick-off annihilation describes the 2-γ annihilation of the e^+ in the Ps with an external spin-antiparallel e^- during collisions with atoms and molecules. This mechanism can also take place when Ps is emitted into pores and subsequently collides with the pore walls, and reduces the vacuum lifetime down to a value as low as 1 ns [10].

Conversion

Due to interaction with other atoms and molecules, the o-Ps can exchange its spin-parallel e^- to a spin-antiparallel e^- and thus become a p-Ps and vice versa. This effect is mainly observed in transition metals with unpaired e^- and paramagnetic substances [20]. At fast conversion rates, the annihilation rate approaches the value

$$\lambda = \frac{1}{4}\lambda_{p-Ps} + \frac{3}{4}\lambda_{o-Ps}, \tag{2.9}$$

with λ_{p-Ps}, λ_{o-Ps} being the annihilation rates of the singlet and triplet state, respectively [21]. Using $\lambda_{Ps} = \frac{1}{\tau_{Ps}}$ with the lifetimes stated above, the minimum lifetime attributed to Ps conversion processes is therefore approximately 500 ps.

Further mechanisms reducing the ortho-Ps lifetime are chemical and magnetic quenching [20]. In Table 2.1, the physical properties of the Ps-atom are summarized.

Table 2.1: Properties of p-Ps and o-Ps.
m_e ... electron restmass
a_0 ... Bohr radius

	p-Ps [$^1S_0$]	**o-Ps [$^3S_1$]**
Mass	$2m_e$	
Radius	$2a_0$	
Charge	neutral	
Binding energy	6.8 eV	
Spin	S = 0 $m_s = 0$	S = 1 $m_s = 0, \pm 1$
Formation	25 %	75 %
Decay	2γ	3γ
Vacuum lifetime	125 ps	142 ns

2.2.1 Negative Positron and Positronium Work Function

The positron work function Φ_+ plays an important role for Ps formation mechanisms and shall therefore be explained briefly. The positron work function is the analogue to the electron work function and describes the amount of energy needed to lift a e^+ from the bulk into the continuum above vacuum level. In case of a *negative* e^+ work function, no energy is needed to eject the e^+. Instead, the positrons even *gain* energy ($\approx |\Phi_+|$ [2]) while being ejected from the material. Depending on the material, the ejected positrons then show energies on the order of 1 eV [22].

It was shown that the negative positron work function is a surface process [1]. Due to the extension of the electron cloud outside the surface of a metal (electron leakage), a dipole layer is formed since residual positive charge of the ionic cores is left behind in the metal [23]. This surface dipole layer and the positron-ion interaction both act repellingly and contribute to the favored ejection of the positrons in negative work function metals [24].

Furthermore, it was shown that for metals, the positronium work function is always smaller than the positron work function, i.e. $\Phi_{Ps} < \Phi_+$ [2, 24].

Since the positron work function is a surface phenomenon, it is expected to be very sensitive to the surface condition. Adsorbed gases, the purity of the metal etc. are expected to play a major role [1].

2.2.2 Ps Formation at Metal Surfaces using Foil Sources

Due to frequent collisions of the positron with conduction electrons and because of the volume exclusion effect of the ionic cores, no Ps can be formed within the metallic bulk [7]. However, different mechanisms can lead to Ps formation, when a thermalized positron reaches the surface:

- Direct emission of Ps due to positron emission and subsequent electron capture in the near surface region, just beyond the top atomic layer [2, 7, 25]. This process is often competing with bare e^+ emission for metals with a negative positron work function.
- Trapping of a e^+ in a surface state and subsequent thermally activated detrapping as Ps [2, 6].

In the first case, the condition for Ps formation is

$$\Phi_{Ps} = \Phi_- + \Phi_+ - E_B \leq 0, \tag{2.10}$$

i.e., the Ps work function is negative [2]. Here, $\Phi_\pm$ denote the electron and positron work functions, respectively, and E_B is the Ps binding energy of $E_B = 6.8\,\mathrm{eV}$ [6]. Note that materials with positive positron work function but negative Ps work function do exist.

In the latter case, the trapped e^+ can either annihilate with a typical lifetime of $\tau \approx 500\,\mathrm{ps}$ [2], or be preferably expelled as Ps. In order to escape as Ps, an electron has to be taken out of the metal and the binding energy of the positron at the surface has to be overcome, while the Ps binding energy is gained. The activation energy for the thermal desorption as Ps is therefore [2, 6]

$$E_A = \Phi_- + E_S - E_B, \tag{2.11}$$

where Φ_- is the electron work function, E_S is the surface state binding energy with respect to vacuum ($E_S \approx 3\,\mathrm{eV}$, depending on the material [6]) and E_B is the binding energy of the Ps-atom, i.e., $E_B = 6.8\,\mathrm{eV}$. Because of the rather high value of E_B ($E_B > \Phi_-$), the

activation energy for Ps emission will normally be lower than the activation energy for bare e^+ emission ($E_{A,e^+} = E_S$). Thus, Ps emission is the energetically more favorable process happening due to thermal fluctuations [2].

It is important to note that also voids and pores contribute to the surface of the material and thus for negative positronium work function metals it should be energetically favorable for positronium to be formed inside voids and pores [24].
It should be mentioned that the mechanisms leading to the branching ratio between positron and positronium emission as well as surface state formation are only partly understood [25].

2.3 Positron Annihilation Lifetime Spectroscopy

As was discussed in Section 2.1, the positron annihilation rate for a homogeneous electron gas is directly proportional to the electron density n, i.e.,

$$\lambda = \tau^{-1} = r_0^2 \pi c n. \tag{2.12}$$

In practice, the annihilation rate will be given by the overlap of the positron density, being the absolute square of the positron wave function $\psi_+(\mathbf{r})$ and the electron density $n_-(\mathbf{r})$

$$\lambda = r_0^2 \pi c \int |\psi_+(\mathbf{r})|^2 n_-(\mathbf{r}) \gamma d\mathbf{r}, \tag{2.13}$$

where r_0 is the classical electron radius, c is the speed of light, $\mathbf{r}$ is the position vector and γ is the enhancement factor, describing the enhancement of the electron density in the proximity of the positron due to Coulomb attraction [20].

At defects, e.g. vacancies, positively charged cores are missing, resulting in an attractive negative potential for positrons. The number of lifetime components that will be measured, correspond to the number of sites the positrons annihilate from. In a perfect crystalline material, there will be only one positron lifetime, the so-called bulk-lifetime τ_b. However, if crystal defects are present, additional, longer lifetimes can be expected, since positrons being trapped in a defect are surrounded by less electrons, i.e., are located at a site with a lower electron density. This leads to a smaller annihilation rate which in turn corresponds to a longer lifetime (compare (2.12)).

The two-state trapping model describes positron trapping and annihilation in a material with only one defect species [14]. The rate equations are given by

$$\frac{dn_b(t)}{dt} = -\lambda_b n_b(t) - \kappa_d n_b(t), \tag{2.14}$$

$$\frac{dn_d(t)}{dt} = -\lambda_d n_d(t) + \kappa_d n_b(t), \tag{2.15}$$

where $n_b(t)$ and $n_d(t)$ are the number of positrons in the bulk and in the defect at time t, λ_b and λ_d are the annihilation rates in the bulk and in the defect, respectively, and κ_d is the trapping rate into the defect.

The solution of the two differential equations is the positron decay spectrum $D(t)$,

$$D(t) = I_1 \exp\left(-\frac{t}{\tau_1}\right) + I_2 \exp\left(-\frac{t}{\tau_2}\right), \tag{2.16}$$

where I_1 and I_2 describe the intensities of the lifetimes τ_1 and τ_2. These parameters are abbreviations for

$$\tau_1 = \frac{1}{\lambda_b + \kappa_d}, \tag{2.17}$$

$$\tau_2 = \frac{1}{\lambda_d}, \tag{2.18}$$

$$I_1 = 1 - I_2, \tag{2.19}$$

$$I_2 = \frac{\kappa_d}{\lambda_b - \lambda_d + \kappa_d}. \tag{2.20}$$

Note that unlike the defect attributed lifetime τ_2, the bulk lifetime cannot be measured directly if defects are present; the experimentally obtained value is lower because of the seemingly higher annihilation rate due to positron trapping, $\lambda_1 = \lambda_b + \kappa_d$ (compare (2.17)).

Since a number of positrons is measured per time channel, the experimentally observed spectrum is

$$N(t) = \left|\frac{dD(t)}{dt}\right| = \sum \frac{I_i}{\tau_i} \exp\left(-\frac{t}{\tau_i}\right). \tag{2.21}$$

The experimental setup is explained in detail in Chapter 4. In order to extract the lifetimes and intensities from a measured positron lifetime spectrum, a model function has to be fitted to the measured spectrum. This is described in the following section.

2.3.1 The Lifetime Analysis Software PALS*fit*

In order to analyze the recorded positron lifetime spectra and extract lifetimes and intensities, the software PALS*fit* was used throughout this work. In this section, the principle behind this routine shall be explained briefly. For more detailed information, especially concerning the fitting algorithms, see Ref. [26].

In PALS*fit*, the least-squares criterion is used. A model function with k parameters $b_1, \ldots, b_k$ is fitted to the measured spectrum such that it minimizes

$$\Phi \equiv \sum_{i=1}^{n} w_i (y_i - f_i(b_1, \ldots, b_k))^2, \tag{2.22}$$

where f_i is the value of the model function corresponding to the measurement point y_i of n data points and w_i is a weighing factor[1].

The model function $f(\tau)$ is considered as a sum of k_0 decaying exponentials a_j, each corresponding to a certain lifetime, convoluted with the resolution function $R(\tau)$ of the lifetime spectrometer. In practice, there will also be a background B, which is superimposed onto the spectrum. This leads to the following expression for the model function

$$f(\tau) = \sum_{j=1}^{k_0} (a_j * R)(\tau) + B, \tag{2.23}$$

with

$$a_j(\tau) = \begin{cases} A_j \exp\left(-\frac{\tau - T_0}{\tau_j}\right), & \tau > T_0 \\ 0, & \tau < T_0. \end{cases} \tag{2.24}$$

In (2.24), T_0 is the so-called time-zero, the onset time for the decaying exponentials, A_j is a pre-exponential factor and τ_j is the lifetime of the j-th component. As can be verified easily, the area below the j-th exponential decay function a_j is given by

$$\int_{T_0}^{\infty} a_j = A_j \tau_j, \tag{2.25}$$

and corresponds to the intensity of the lifetime τ_j.

The resolution function $R(\tau)$ in (2.23) is described by a sum of k_g Gaussians $G_p(\tau)$,

$$R(\tau) = \sum_{p=1}^{k_g} \omega_p G_p(\tau). \tag{2.26}$$

[1] Statistical weighing is used, i.e., $w_i = \frac{1}{s_i^2}$ where s_i^2 is the variance of y_i.

Here, ω_p is the amplitude (or intensity) of the p-th Gaussian with the constraint $\sum_{p=1}^{k_g} \omega_p = 1$, and

$$G_p(\tau) = \frac{1}{\sqrt{2\pi}\sigma_p} \exp\left(-\frac{(\tau - \Delta_p)^2}{2\sigma_p^2}\right). \tag{2.27}$$

In (2.27), Δ_p is the point around which the p-th Gaussian is centered, i.e., the shift with respect to the Gaussian which is chosen to be located at $\Delta = 0$, and σ_p is the standard deviation of the p-th Gaussian which is directly linked to the **F**ull **W**idth at **H**alf **M**aximum (FWHM) of the corresponding Gaussian via $\mathrm{FWHM}_p = 2\sqrt{2\ln 2}\ \sigma_p$.

In order to decide whether a fit result describes the spectrum properly, the variance of the fit, also called reduced-chi-square, is calculated by the program. It is defined as

$$var = \frac{\Phi_{min}}{n - k_{free}}, \tag{2.28}$$

where n is the number of data values (= number of fit channels) and k_{free} is the effective number of free parameters in the analysis. A value close to unity is indicative for a good fit result [26].

ResolutionFit and PositronFit

PALS*fit* works in two modi. The first one is called *ResolutionFit* and primarily helps to determine the resolution function of the spectrometer. Typically, a standard sample with only one distinct lifetime will be analyzed to determine the resolution function. The fitting parameters in *ResolutionFit* are the widths (FWHM) and shifts (Δ) of the Gaussians, the lifetimes τ_j, the corresponding relative intensities I_j and the time-zero T_0.

Once the resolution function is determined, it can subsequently be used in the second mode *PositronFit*. Here, the parameters concerning $R(\tau)$ are fixed, while a chosen number of lifetimes τ_j with corresponding intensities I_j and time-zero T_0 are fitted.

2.3.2 The Mean Positron Lifetime τ_m

A mean positron lifetime can be calculated from the obtained lifetimes τ_i and the corresponding intensities I_i, i.e.,

$$\tau_m = \sum_{i=1}^{k_0} \tau_i I_i, \tag{2.29}$$

where k_0 is the number of lifetime components. This mean lifetime is a statistically very accurate parameter and largely cancels the ambiguities in the spectrum decomposition [17].

CHAPTER 3

Synthesis and Characterization of Nanoporous Platinum

3.1 Fundamentals of Electrochemical Dealloying

Dealloying is the selective dissolution (etching) of one or more less noble components out of an alloy. A nanoporous sponge-like structure with a high specific surface area is left behind, exhibiting interconnected pores as well as ligaments consisting almost entirely of the noble component (bicontinuous ligament-pore structure) [27, 28]. A premise for a working dealloying process with porosity formation is a single-phase solid solution starting alloy [29]. The dealloying process is triggered by applying a driving force to the system. This driving force can be an applied voltage between the alloy and a reference electrode, or the presence of oxidizing species in the electrolyte surrounding the alloy [29].

Erlebacher et al. developed a kinetic Monte Carlo model to simulate dealloying in an Ag-Au alloy, reproducing morphological and kinetic trends found in experiments [27]. Although the model was developed for Ag-Au, the considerations hold for any dealloyable system. The physical effects incorporated in the model are diffusion of the alloy constituents as well as dissolution of the less noble component. The dealloying process starts with the dissolution of one Ag atom at a flat surface of the alloy. This leaves behind a vacancy, exposing less coordinated Ag atoms to the electrolyte. As they are dissolved, Au atoms are left behind on the underlying surface and start to diffuse and agglomerate due to surface energy minimization. As the process continues, the surface consists of Au clusters and regions with the initial alloy composition. As more Ag is dissolved, more Au is released

onto the surface and the clusters grow or new clusters are formed if energetically more favorable. While the peaks of the clusters are rich in Au, the bases of the clusters still show alloy composition, leading to undercutting of the clusters due to dissolution of Ag at the base. The described process leads a growth in surface area due to pit formation and ultimately to the porous, interconnected structure [27], see Figure 3.1.

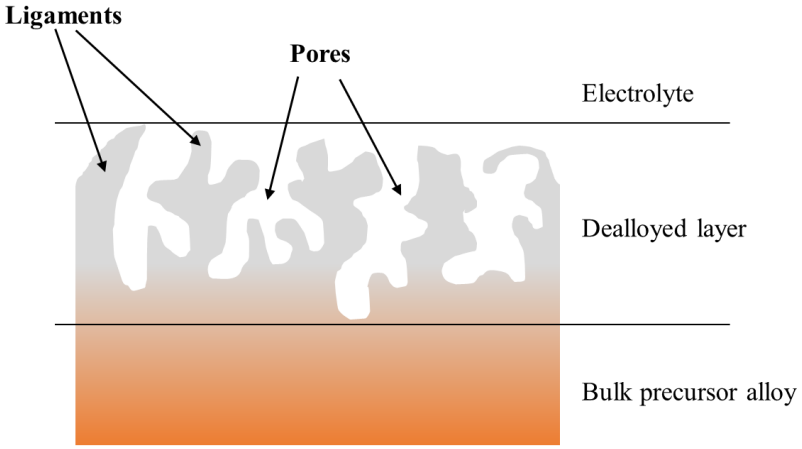

Figure 3.1: During the dealloying process, pores are formed due to the selective dissolution of the less noble component. Ligaments, rich in the noble component, are left behind. Drawn after [30].

Two important, alloy-specific parameters for the formation of nanoporous structures by dealloying are the parting limit p and the critical potential V_C.

The parting limit p in an alloy A_pB_{1-p} is the percentage of the less noble component A in the alloy below which no dealloying can occur. The minimum value for p depends on the dissolution rate of A as well as on the surface diffusivity of B [31]. Typical values for p are 60-80 at.% [29].

The critical potential V_C is the potential that has to be applied in order to start sustainable dealloying. It is characterized by the onset voltage of a strongly rising current in potential sweep measurements $I(V)$ (polarization scans)[2]. Another, more accurate possibility to determine the critical potential, is to conduct potential hold measurements. Here, a potential with respect to a reference electrode is applied and the current is measured over time. In potential hold measurements below the critical potential ($V < V_C$), the current continuously decays while for $V > V_C$ an increase in dealloying current can be observed [28].

[2] The first peak in potential sweep measurements develops due to the dissolution of the less noble component from the first surface layers. It is followed by the passivation region. The second increase in current at higher voltages marks the dissolution of the less noble component from inside the alloy. The corresponding voltage thus is the critical potential for dealloying [28].

At $V < V_C$ and/or at alloy compositions below the parting limit, the surface of the alloy is passivated by the noble component and no dealloying takes place [28]. In addition to alloy composition and applied voltages also dealloying time, dealloying temperature and the electrolyte used influence the resulting nanoporous structure [32].

For the alloy $Cu_{75}Pt_{25}$ (at.%) used in this work, Pugh et al. determined the critical potential, depending on where the onset of the rising dealloying current is seen, as $V_C = 730\,\text{mV}$ vs. NHE (534 mV vs. Ag/AgCl) [33], $V_C = 842\,\text{mV}$ vs. NHE (645 mV vs. Ag/AgCl) [29], respectively.
Due to the extremely low values for the surface diffusivity of Pt ($10^{-22}\,\text{cm}^2\text{s}^{-1}$ [28]), the pores in a $Cu_{75}Pt_{25}$ dealloying experiment in 1-M H_2SO_4 at $V = 1444\,\text{mV}$ vs. NHE (1245 mV vs. Ag/AgCl) for 2.4 h exhibit diameters of 3.5 to 4 nm [29]. A FESEM image of the resulting nanoporous structure in the as-dealloyed state as well as after annealing at $T = 500\,^\circ\text{C}$ can be found in Ref. [29].

3.2 Experimental Methods

During this work, the method of chrono amperometry (see Section 3.2.1) was used for dealloying of the $Cu_{75}Pt_{25}$ alloy samples. Cyclic voltammetry, as explained in Section 3.2.2, was used to determine the specific surface area of the samples.

All electrochemical measurements were conducted in a three-electrode geometry, i.e.,

- Working electrode (WE)
- Reference electrode (RE)
- Counter electrode (CE).

The working electrode is the sample under investigation. All potentials that are applied to the working electrode are measured versus the reference electrode, which marks the zero-potential in the respective experiment. However, apart from leakage current, no current can flow between working electrode and reference electrode due to the high impedance of the reference electrode. Therefore a third electrode, the counter electrode, is needed to allow for current flow.
During all conducted measurements, a Metrohm Autolab Potentiostat (PGSTAT 128N) was used in combination with the program NOVA 1.10 to collect the data.
An Ag/AgCl reference electrode (3-M KCl) from the company Metrohm Autolab was used.

If not stated otherwise, all potentials within this work are quoted with respect to this electrode.

In the chrono amperometry experiments (dealloying), a tungsten rod was used as counter electrode and 1-M H_2SO_4 served as electrolyte. A dealloying potential of $V = 1175\,\mathrm{mV}$ vs. Ag/AgCl was applied to the working electrode. Figure 3.2 shows the electrodes used before immersion into the electrolyte.

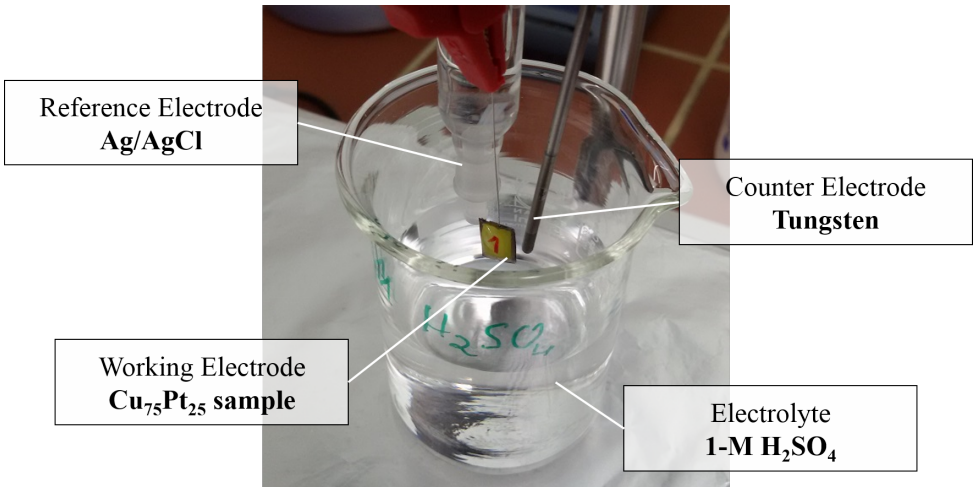

Figure 3.2: Picture of the electrochemical cell used for dealloying of $Cu_{75}Pt_{25}$. Electrolyte: 1-M H_2SO_4. CE: Tungsten rod. RE: Ag/AgCl.

In cyclic voltammetry measurements, a carbon fabric with high surface area (company Epcos) was used as counter electrode and 1-M KOH as electrolyte.

3.2.1 Chrono Amperometry (CA) - Dealloying

In chrono amperometry measurements, a constant potential is applied to the working electrode and the current is measured as a function of time. This approach was used for dealloying experiments throughout this work.

From the weight of the $Cu_{75}Pt_{25}$ samples before dealloying, the charge that is expected to accumulate during the complete removal of Cu can be calculated. To receive a value for the expected charge per 1 g of the master alloy, the number of atoms in 1 g has to be calculated first. From

$$N = \frac{1}{(0.75 \cdot m_{Cu} + 0.25 \cdot m_{Pt})}, \tag{3.1}$$

and with $m_{Cu} = 63.546\,\mathrm{u}$, $m_{Pt} = 195.084\,\mathrm{u}$ and $\mathrm{u} = 1.660538921 \cdot 10^{-24}\,\mathrm{g}$, the number of atoms N in 1 g $Cu_{75}Pt_{25}$ master alloy equates to

$$N = 6.24506 \cdot 10^{21}\,{}^{\text{atoms}}/_{1\text{g } Cu_{75}Pt_{25}}.$$

Cu is known to dissolve in the form of Cu^{2+} [34]. It is additionally assumed that during the dealloying process, which rearranges the more noble component due to surface diffusion, each Pt atom will eventually adsorb one O^{2-} ion and become PtO.

The expected charge is therefore

$$Q = (N_{Cu} + N_{Pt}) \cdot 2e \tag{3.2}$$

$$= N \cdot 2e \tag{3.3}$$

$$\approx 2001\,{}^{\text{As}}/_{1\text{g } Cu_{75}Pt_{25}}. \tag{3.4}$$

3.2.2 Cyclic Voltammetry (CV)

In cyclic voltammetry experiments, the potential between working electrode and reference electrode immersed into an electrolyte is ramped linearly from a lower voltage to a higher voltage and back again. The resulting current $I(U)$ between the working electrode and the counter electrode is recorded as a function of the applied voltage.

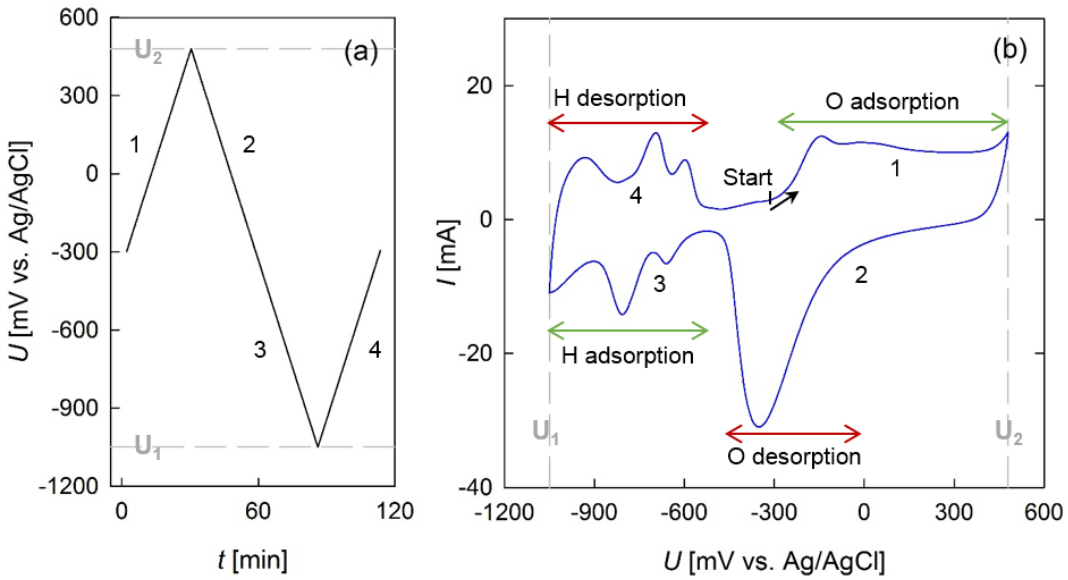

Figure 3.3: Cyclic voltammetry exemplarily shown for a Pt-pellet. (a) The linear scan of the potential is shown ($v = 0.5\,{}^{\text{mV}}/_{\text{s}}$). (b) Cyclic voltammogram of Pt in 1-M KOH. H and O ad- and desorption peaks as well as the upper and lower potential limit U_2 and U_1 are labelled in the figure.

Figure 3.3a shows the applied potential $U(t)$ as a function of time and Figure 3.3b depicts

the resulting cyclic voltammogram $I(U)$ shown here for a Pt-pellet. Different electrode ad- and desorption peaks as well as regions with almost constant current, corresponding to double layer charging, can be observed in Figure 3.3b.

An important parameter in cyclic voltammetry experiments is the scan rate, i.e.,

$$v = \frac{dU}{dt}. \tag{3.5}$$

Especially for porous samples with high surface areas, a low scan rate on the order of 1 $^{\mathrm{mV}}/_{\mathrm{s}}$ is needed, because the kinetics of slow processes cannot be resolved properly if the potential is changed too quickly. Furthermore, when recording a cyclic voltammogram with porous samples it is important to use a counter electrode exhibiting a high surface area. This guarantees that processes on the counter electrode do not limit the current.

3.2.2.1 Determination of the Specific Surface Area from Cyclic Voltammograms

To determine the specific surface area of a sample from a cyclic voltammogram, the charge associated with hydrogen desorption at the working electrode is determined from the voltammogram and compared to the known value of the specific charge-per-unit-area associated with the desorption. Under the assumption that one H atom is adsorbed (desorbed) per Pt atom, a value of $q_H = 210\,^{\mu\mathrm{C}}/_{\mathrm{cm}^2}$ has been reported by Trasatti and Petrii and can be understood as a mean charge-per-surface value for the main low-index surfaces of polycrystalline Pt [35].

To obtain the charge that corresponds to the desorption of the H-monolayer, the area below the hydrogen desorption peak $\int I dU$, which is corrected for double layer charging, is determined (see Figure 3.4). This value is then divided by the scan rate and results in the charge Q_H that accumulated on the electrochemically active surface[3]

$$Q_H = \int I dt = \int \frac{I dU}{\frac{dU}{dt}}. \tag{3.6}$$

As depicted in Figure 3.4, the baseline of the capacitive double layer charging was assumed to be linear. The specific surface area A_{spec} can then be obtained by dividing the total charge corresponding to the hydrogen desorption Q_H, by the value for q_H and the mass m of the sample.

$$A_{spec} = \frac{Q_H}{q_H m}. \tag{3.7}$$

The inaccuracy related to this method is reported to be about 10 % [35].

[3] This implies that with this method closed pores yield no surface contribution.

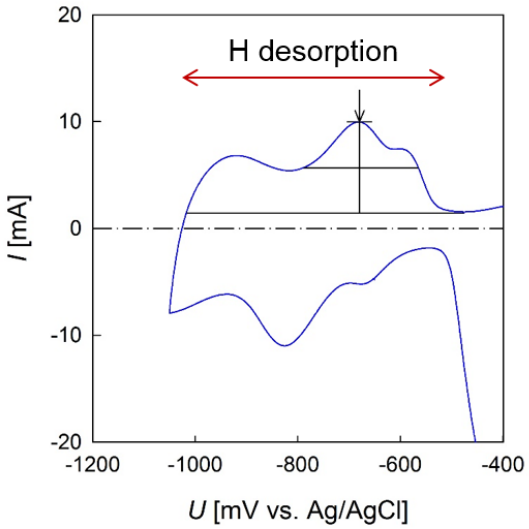

Figure 3.4: The area that is used to determine the charge due to hydrogen desorption is marked in black. Note that the baseline has an offset > 0 in order to correct for capacitive charge due to double layer charging.

3.2.3 Different Experimental Approaches for Dealloying of $Cu_{75}Pt_{25}$

For the investigation of nanoporous Pt by means of positron annihilation, the samples should exhibit the following features:

- Maximum specific surface area due to high copper dissolution
- Reasonable robustness for sample handling.

For the first tries of electrochemical dealloying of $Cu_{75}Pt_{25}$, pieces of approximately (3×10) mm and a thickness of $180\,\mu$m were used and contacted in different ways in order to find a suitable design that fulfills the requirements stated above. Figures 3.5a - 3.5e show the different designs. It turned out that for sample handling it is advantageous to attach some kind of mechanical support to one side of the sample (backbone), because the samples are extraordinarily brittle (especially when the oxygen that forms during the dealloying process is reduced). Otherwise, it is almost impossible to undertake measurements without breaking the samples (Figure 3.5a).
As backbone, we used Crystalbond 509 Amber from AREMCO Products (Figures 3.5b - 3.5e) that we melted and applied to the sample. However, applying Crystalbond directly onto the platinum wire led to contact problems, since bond material can reach below the wire (Figure 3.5b). Therefore, an adhesive tape was used to establish a good contact between

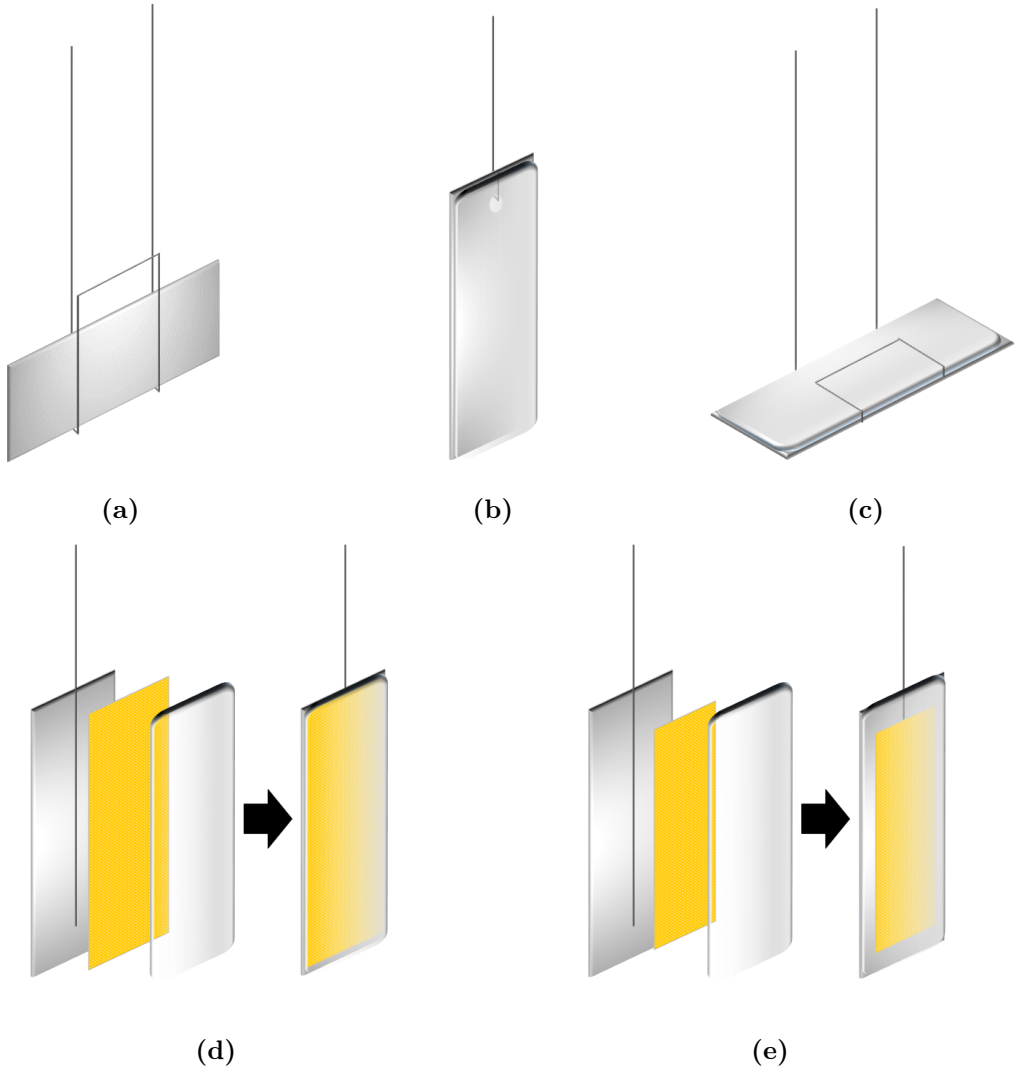

Figure 3.5: Different contact designs for dealloying of $Cu_{75}Pt_{25}$. (a) Contact is established via a platinum wire swing. (b) Contact via a platinum wire hook. Crystalbond was used as backbone. (c) Contact via a platinum wire swing with Crystalbond as backbone for the alloy. (d) Stack of alloy, flattened Pt-wire, sample-sized adhesive tape, Crystalbond. (e) Stack of alloy, flattened Pt-wire, *small* adhesive tape, Crystalbond. Only design (e) fulfilled the requirements of high copper dissolution and overall robustness.

the alloy and the wire. The contact was further enhanced by flattening the platinum wire at the contacting end. On top of the adhesive tape, the Crystalbond again served as backbone (Figures 3.5d and 3.5e). However, if the adhesive tape has the same dimensions as the sample (Figure 3.5d), the electrolyte can reach below the tape at the edges and intrude along the wire, which again leads to contact problems after some time of dealloying. Therefore it is important to use an adhesive tape smaller than the dimensions of the alloy (Figure 3.5e). This design was used for further experiments.

3.2.4 Synthesis of Nanoporous Pt via Dealloying of $Cu_{75}Pt_{25}$

The $Cu_{75}Pt_{25}$ master alloys (at.%) were prepared by the group of Prof. Weißmüller at the Institute of Materials Research, Helmholtz-Zentrum Geesthacht. The alloys were arc-melted from high purity Cu (99.99 + %) and Pt (99.99 %) wires and then homogenized for 4 h at a temperature of 1000 °C. Foils of approximately 180 μm and 300 μm were obtained by cold rolling. Between the rolling steps and afterwards, the samples were annealed twice for 1 h at 700 °C.

For the dealloying procedure, pieces of the alloy were cut to a size of approximately $6 \times 6\,\mathrm{mm}^2$ with the help of a low-speed diamond saw (rotational speed: ≈ 80 rpm; weight: 50 g). Figures 3.6a - 3.6c show how the samples were prepared for the dealloying process following the design idea presented in Figure 3.5e.

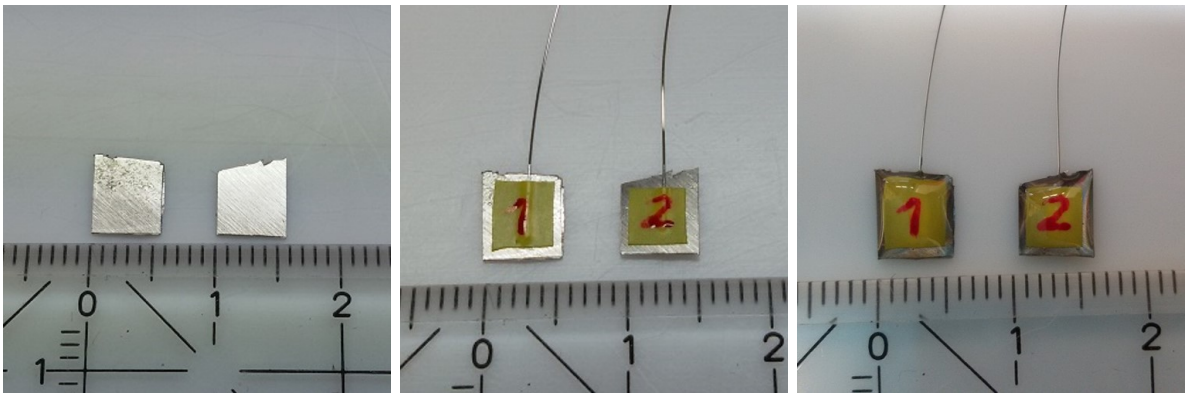

(a) **(b)** **(c)**

Figure 3.6: (a) The two $Cu_{75}Pt_{25}$ samples are cut to a size of $\approx (6 \times 6)\,\mathrm{mm}^2$. (b) A 0.2 mm thick platinum wire is attached to the $Cu_{75}Pt_{25}$ samples with adhesive tape. (c) Acid-resistant Crystalbond is used to seal the samples.

An approximately 4 cm long, 0.2 mm thick platinum wire (99.9 % purity) from Chempur (Karlsruhe, Germany) was used to contact the samples. In order to enhance the contact

area, the lower part of the wire was flattened and subsequently stuck to the samples using insulating tape (Figure 3.6b). Crystalbond was melted with an electrical stove and added to the backside of the sample (Figure 3.6c). Care has to be taken in order to properly seal the sides of the samples, so that no electrolyte can reach below the insulating tape which could lead to contact loss.

Subsequently, the front sides were cleaned cautiously using acetone in order to remove potential Crystalbond residues which would limit the area active for dealloying. Apart from that, for successive positron lifetime measurements, the surface should not be contaminated by unknown substances.

Figure 3.7a shows the electrodes during the dealloying process. The counter electrode shows copper deposition. For samples where the current dropped to zero before the achieved charge was satisfactory, a contact problem at the interface between wire and porous metal was seen as reason. In these cases, the samples were re-contacted from the front side using a platinum 'wire-swing' (see Figure 3.7b).

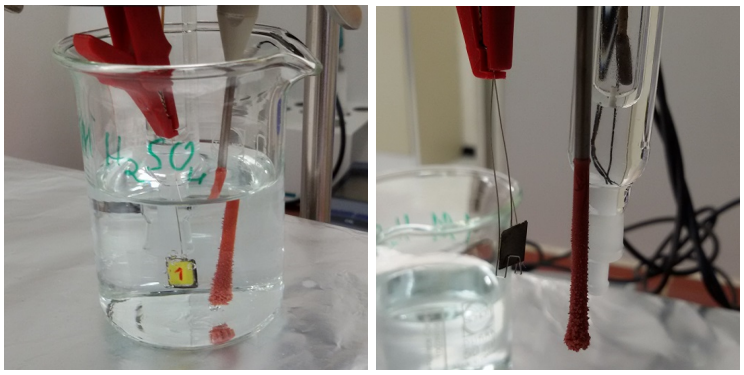

(a) **(b)**

Figure 3.7: (a) Electrodes after a dealloying process. Electrolyte: 1-M H_2SO_4. WE: $Cu_{75}Pt_{25}$. CE: Tungsten rod. RE: Ag/AgCl. Copper is deposited at the counter electrode. (b) For samples with unsatisfactory copper dissolution at the end of the dealloying process, a new contact was established from the front side using a Pt 'wire-swing'.

During this work, two sample pairs were fabricated via dealloying (compare Section 3.3). The specimens with a thickness of approximately 180 μm and 300 μm, respectively, shall be labelled np-Pt180 and np-Pt300 throughout this work.

The mean positron penetration depth as described in Section 2.1.2 can be estimated as $\approx 38\,\mu$m for the dealloyed samples (source: ^{22}Na)[4].

[4] The mean density of the dealloyed samples can be estimated via the fcc lattice constant of the $Cu_{75}Pt_{25}$ alloy, i.e., $a = 0.368$ nm [36]. Under the assumption that the macroscopic volume remains constant while the copper is dissolved, the mean density results in $\rho_{np-Pt} = \frac{1}{a^3} \cdot 4 \cdot \frac{1}{4} \cdot m_{Pt}$, i.e., $\rho_{np-Pt} = 6.5\,\mathrm{g/cm^3}$.

3.2.5 Synthesis of Nanoporous Pt via Powder Compaction

Two Pt-pellets were fabricated using nanocrystalline platinum powder (Platinum black, Chempur) with a nominal specific surface area of 20 to 40 $\mathrm{m^2/g}$. During this work, these samples shall be labelled Pt-pellet 1 and 2, respectively. The powder, with crystallite sizes of 4 to 7 nm, was compacted into pellets with a diameter of 8 mm using an Enerpac P392 hydraulic press. The pressure exerted onto the samples[5] was $\approx 40 \pm 10$ MPa. Afterwards, the pellets were tempered for 12 h in a vacuum furnace ($p \approx 4 \cdot 10^{-6}$ mbar) at 150 °C. The pellets were weighed and the volume was calculated. By comparing the resulting density to the density of Pt, the porosity of the pellets in this as-prepared state was estimated and is listed in Table 3.1.

Table 3.1: Pt pellets compacted from nanocrystalline Pt powder in the as-prepared state. The diameter of the specimens is $d = 8$ mm.

	Pellet 1	**Pellet 2**
Thickness [μm]	660	650
Mass [mg]	164.93	168.45
Density [$\mathrm{g/cm^3}$]	4.9	5.2
Porosity [%]	77	76

The mean positron penetration depth for the fabricated Pt-pellets, as described in Section 2.1.2, can be estimated from the mean density, and is $\approx 50\,\mu$m (source: ^{22}Na).

3.2.6 Sample Treatment

During this work, the fabricated samples were treated in different ways before positron lifetime measurements were conducted. In this subsection, the details of these treatments shall be described while the reasoning behind will be explained together with the respective lifetime measurement (see Chapter 5).

Oxide reduction

The oxide was reduced electrochemically for all three sample pairs. For the samples np-Pt300 and the Pt-pellets, this step was done by choosing a stopping potential of $U =$

[5] The real pressure acting on the sample has a high uncertainty because of the factor 39 due to the ratio of hydraulic press stamp area ($d = 50$ mm) to sample stamp area ($d = 8$ mm). The smallest pressure that can be exerted (1 small unit at the pressure gauge) corresponds to $p = 39$ MPa.

−400 mV in the CV measurements (compare Section 3.4). Note that this potential is smaller than the onset-value for oxygen adsorption on Pt.

The samples np-Pt180 were freed from oxygen using a potential hold method. A constant potential of $U = -650\,\text{mV}$ vs. Ag/AgCl was applied until the current dropped to zero ($\approx 10\,\text{min}$).

Tempering at 150 °C for 12 h, Pt-pellets

The treatment was conducted in a vacuum furnace where the temperature and pressure behaviour was logged in the first hour (see Figure 3.8). The rise in pressure by less than a factor of four is attributed to evaporating residues from the sample chamber wall.

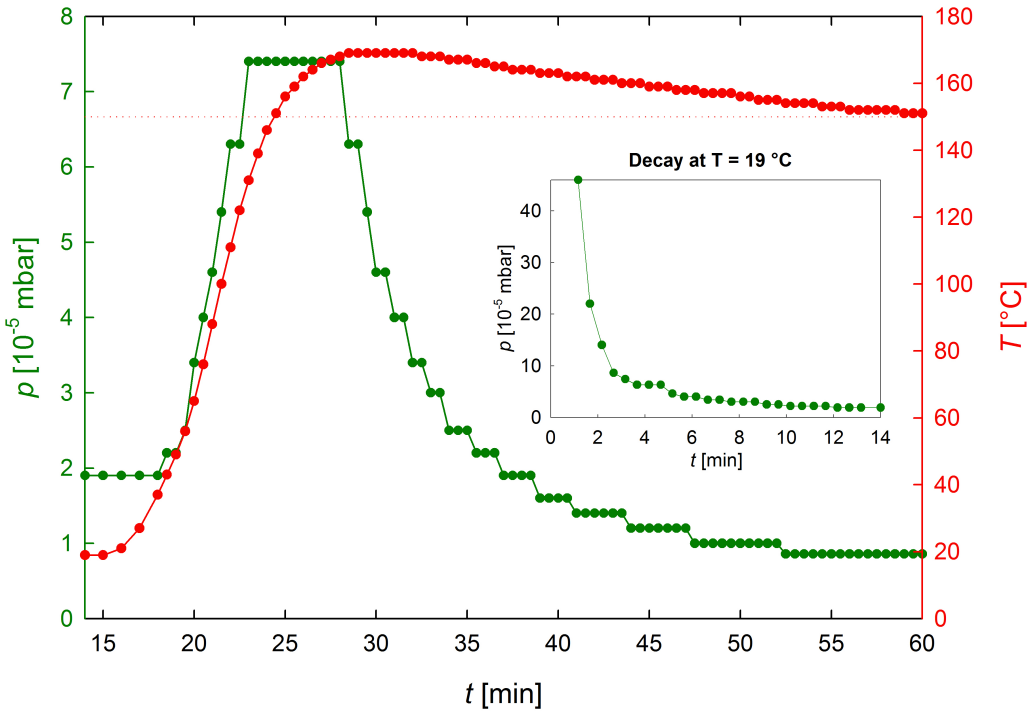

Figure 3.8: Temperature (red) and pressure (green) development for the Pt-pellets tempering treatment. The inset shows the exponential pressure decay at a constant temperature of 19 °C before the heating sequence was started.

Annealing at 500 °C for 30 min, Pt-pellets

This annealing step was executed in a vacuum furnace, where the evacuated sample chamber was inserted into the furnace at at a temperature of 220 °C. The sample was held at 500 °C for 30 min. A drastic shrinkage could be observed for the samples after this annealing step. The porosity was again estimated and is given in Table 3.2 together with other parameters needed for the estimation.

Table 3.2: Pt-pellets after annealing at 500 °C for 30 min.

	Pellet 1	**Pellet 2**
Thickness [μm]	478	515
Diameter [mm]	5.53	5.66
Mass [mg]	157.39	163.25
Density [g/cm^3]	13.7	12.6
Porosity [%]	36	41

Annealing at 500 °C for 30 min, np-Pt300

In order to anneal the nanoporous samples np-Pt300, the Crystalbond first had to be removed. This was done cautiously by storing the specimens in acetone over night. Afterwards, the samples were rinsed with distilled water[6]. As was expected, due to the highly brittle nature of the samples, little pieces broke out during the described steps. After air-drying, the samples were transferred to a preheated furnace and held at T = 500 °C for 30 min. The samples were then cooled at ambient temperature.

The temperature choice and annealing time were adopted from Pugh, who investigated temperature coarsening at np-Pt prepared from $Cu_{75}Pt_{25}$ [12]. According to his work, pore diameters and ligament sizes on the order of 100 nm can be expected after this treatment.

3.3 Results - Dealloying Curves and Accumulated Charge

In this section, the $I(t)$ dealloying curves as well as the accumulated charge $Q(t) = \int I(t)dt$ are presented (see Figures 3.10a - 3.11b). A constant potential of $V = 1175$ mV vs. Ag/AgCl was used during all dealloying experiments.

All measured dealloying curves show the same characteristic $I(t)$ behavior as is depicted in Figure 3.9. A first quick increase in current **(I)** is followed by a decreasing current **(II)**. After a minimum is reached, the current rises again **(III)** and a develops a maximum. Subsequently, the current decays again **(IV)**.

[6] Rinsing the samples with distilled water is very important in order to remove acetone residues from the np-Pt. If the samples are not rinsed, they will very likely catch fire due to the high surface area of the np-Pt and the highly flammable acetone.

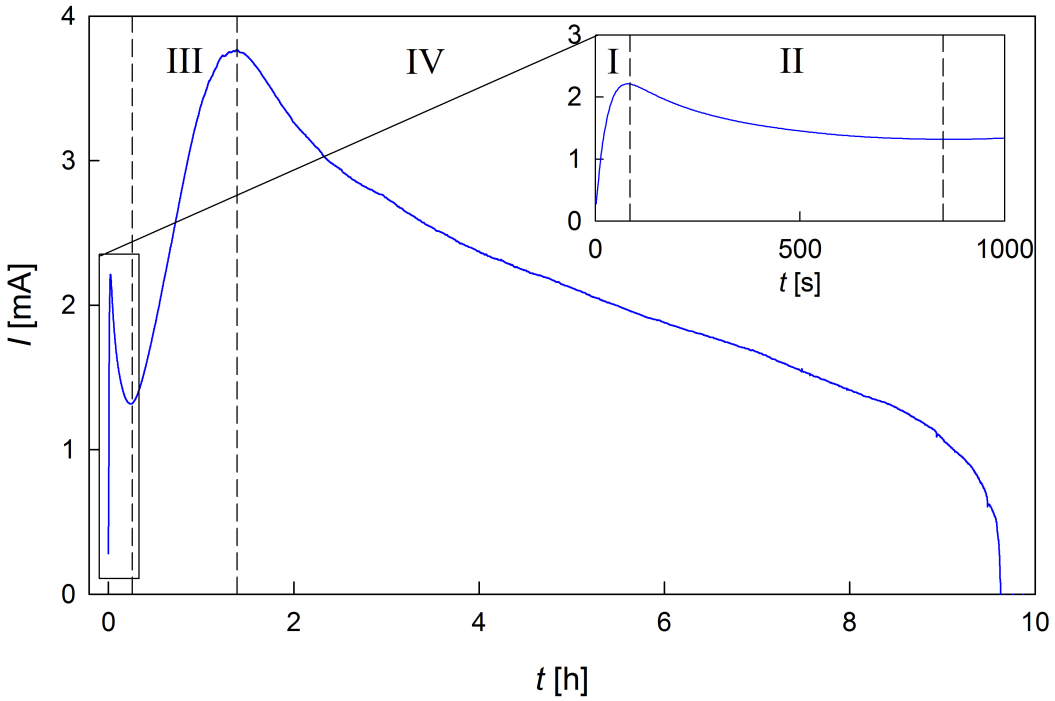

Figure 3.9: Current $I(t)$ for an exemplary dealloying process. The inset shows the first two stages at early times.

These stages are described as follows:

(I): The first increase in current over a timescale of about 1 min is attributed to the dissolution of the less noble component Cu from the first surface layer. As was described in Section 3.1, the process starts with the dissolution of one single Cu atom, leaving behind low coordinated atoms. As more Cu atoms are dissolved from many sites, the number of Cu atoms being susceptible to dissolution increases and the current therefore rises until the first layer is dissolved. This corresponds to the local maximum in the beginning [37].

(II): As only few Cu atoms being exposed to the electrolyte remain, and the more noble component Pt from the uppermost layer starts to agglomerate into clusters, partially passivating the surface, the current decreases again [37].

(III): As Pt atoms diffuse and settle at clusters, the overall surface increases, which leads to hills, rich in Pt at their peaks but with alloy composition at the bases. As a result of the increased surface, Pt atoms cannot passivate these bases anymore. This leads to a mushroom-shaped undercutting of the clusters, resulting in a growing surface area. Consequently, the current rises again [37].

This increasing current was described differently in the doctoral thesis of Pugh as originating from a preferential grain boundary attack [12]. According to this theory, the dissolution of Cu at Cu-rich grain boundaries results in an ingress of electrolyte into the alloy. Therefore, a higher surface area is exposed to the electrolyte which in turn results in higher dealloying currents.

(IV): Pugh stated that once the Cu is dissolved from the grain boundaries, the slower selective dissolution from inside the grains starts and the current decays again. Although the total surface area of the nanoporous metal increases during the dealloying process, the surface being active for dissolution decreases as the copper content declines. Finally the current drops to zero.

In Table 3.3, the expected charges calculated as explained in Section 3.2.1 are given together with the achieved charges and other important parameters concerning the dealloying process of the samples np-Pt180 and np-Pt300.

Table 3.3: Dealloying (DA) of $Cu_{75}Pt_{25}$ samples at $V = 1175\,\text{mV}$ vs. Ag/AgCl and corresponding charges Q.

	np-Pt180		**np-Pt300**	
	1	**2**	**1**	**2**
Thickness [μm]	≈180	≈180	333	282
Weight before DA [mg]	41.60	38.73	109.65	88.94
$\mathbf{Q}_{expected}$ [As]	83.2	77.5	219.4	178.0
$\mathbf{Q}_{1^{st}run}$ [As]	73.9	74.4	153.5	160.3
$\mathbf{Q}_{2^{nd}run}$ [As]	-	-	67.2	19.6
$\mathbf{Q}_{achieved}$ **total** [As]	73.9	74.4	220.7	179.9
$\frac{Q_{achieved}}{Q_{expected}}$ [%]	88.8	96.0	100.6	101.1
$\mathbf{t}_{dealloying}$ [h]	9.6	17.6	34.9	26.4

Figures 3.10a and 3.10b show the dealloying current of the samples np-Pt180-1 and np-Pt180-2. Although the samples are of similar weight and size, specimen 1 shows a value of I_{max} almost twice as high as compared to sample 2. In turn, the time needed to dealloy sample 2 is roughly twice the time needed for sample 1. Due to the smooth current progress, contact problems can be excluded. There is a small, however unlikely possibility that Crystalbond contaminated the frontside during the sample preparation and was not removed entirely, resulting in a smaller electrolyte-exposed surface. About 89 % and 96 % of copper could be dissolved from the samples.

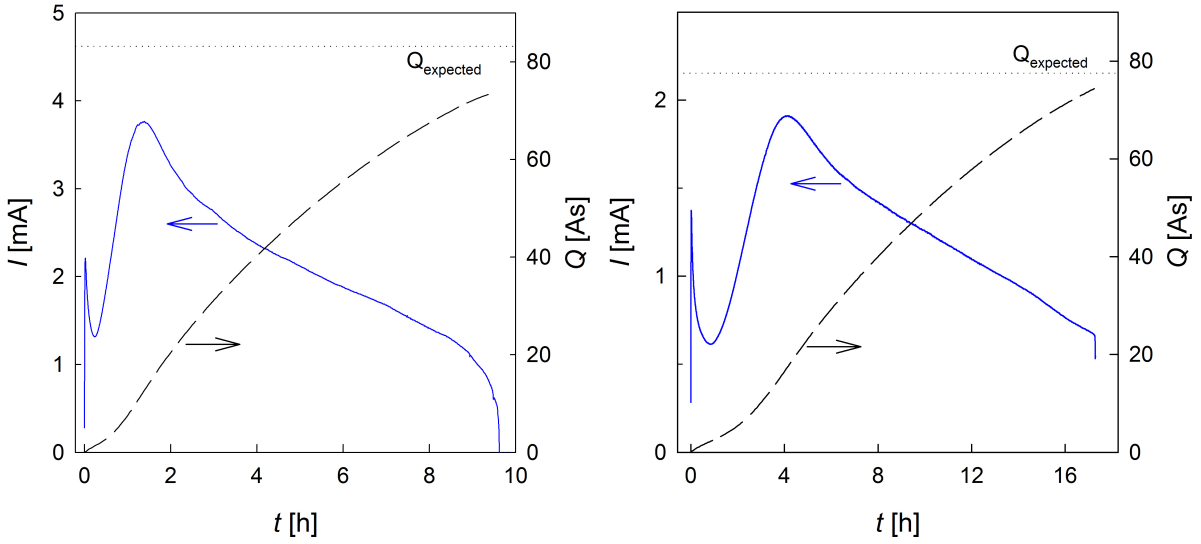

(a) np-Pt180-1 **(b)** np-Pt180-2

Figure 3.10: Dealloying current $I(t)$ (solid blue line) and accumulated charge $Q(t)$ (dashed black line) for the samples np-Pt180-1 (a) and np-Pt180-2 (b).

Figures 3.11a and 3.11b show the dealloying currents and accumulated charges for the samples np-Pt300-1 and np-Pt300-2. Here, the maximum current can be observed to be very similar for both samples. However, after about 14.5 h the contact is lost in the dealloying process of sample np-Pt300-1. In this first run, the achieved charge was only about 70 % of the expected charge for this sample. Therefore, the dealloying process was resumed in a second run, now contacted from the front via a 'wire-swing' (see Figure 3.7b). A cutoff-limit was set to 0.3 mA. The achieved charge of $Q_{np-Pt300-1} = 220.7\,\mathrm{As}$ corresponds to 100.6 % of copper dissolution. Note that the value for dissolution of over hundred percent is a consequence of small leakage currents.

The thinner sample np-Pt300-2 already showed a 90 % copper dissolution after the first run. However, for the sake of uniformity, this sample was also further dealloyed in a second run and an overall dissolution of 101.1 % was achieved.

The current behaviour in the second dealloying run shows an expected decay, which fits well to the one observed in the first run. An initial high current is observed in the beginning of the second run. This can be attributed to Cu atoms that diffused to the surface and are immediately dissolved as the second run is started.

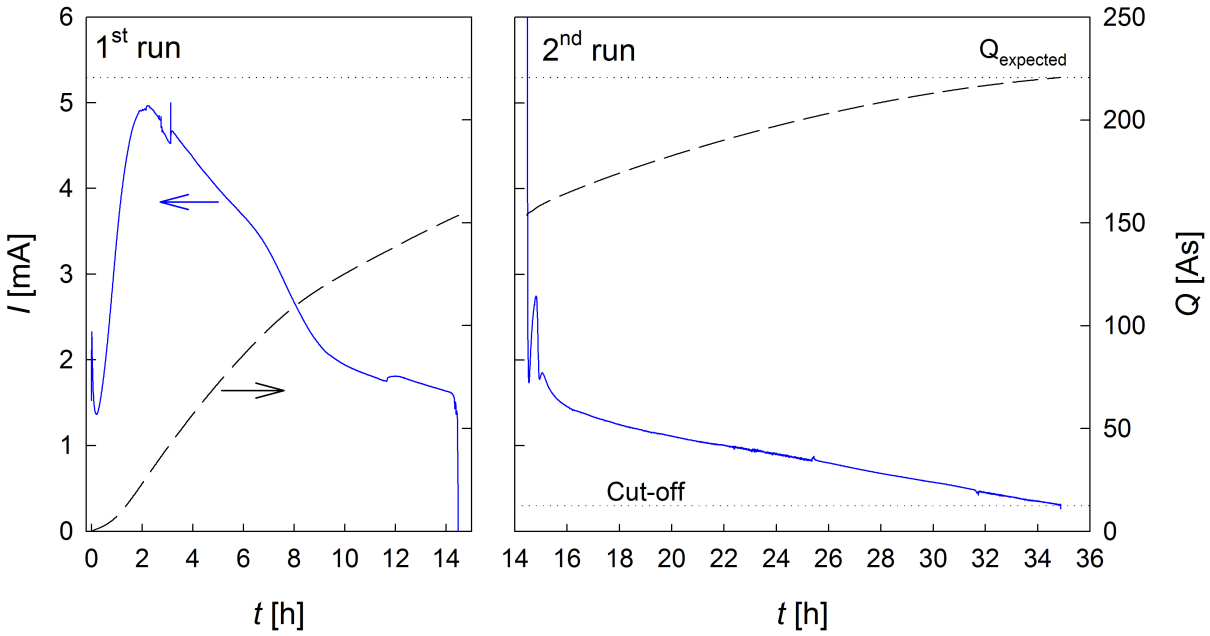

(a) Sample np-Pt300-1.

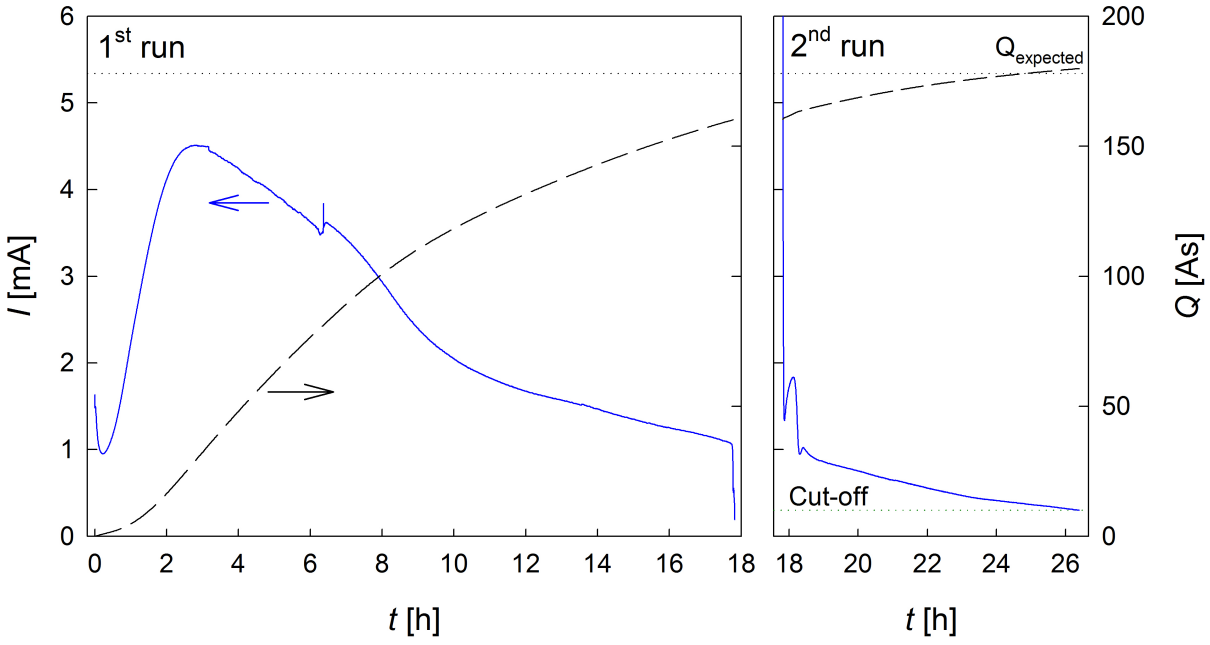

(b) Sample np-Pt300-2.

Figure 3.11: Dealloying current $I(t)$ (solid blue line) and accumulated charge $Q(t)$ (dashed black line) for the samples np-Pt300-1 (a) and np-Pt300-2 (b). During the 1^{st} run, the samples were contacted as described in Section 3.2.4. The contact for the 2^{nd} run was established via a Pt wire-swing.

3.4 Results - Cyclic Voltammetry and Specific Surface Determination

In this section, the results of the cyclic voltammetry experiments are presented. Figure 3.12a and 3.12b exemplarily show a cyclic voltammogram for one of the dealloyed samples (np-Pt300-2) and one of the Pt-pellet samples (pellet 2) in the as-prepared state. The voltammograms were recorded in a potential range between $U_1 = -1050\,\mathrm{mV}$ and $U_2 = 480\,\mathrm{mV}$ vs. Ag/AgCl. The scan rate was $0.5\,\mathrm{mV/s}$ and four cycles were recorded. The start potential was chosen as $U_{Start} = -300\,\mathrm{mV}$. Note that the stop potential $U_{Stop} = -400\,\mathrm{mV}$ has a value smaller than the onset for oxygen adsorption. Thus after cycling, the sample oxide is reduced.

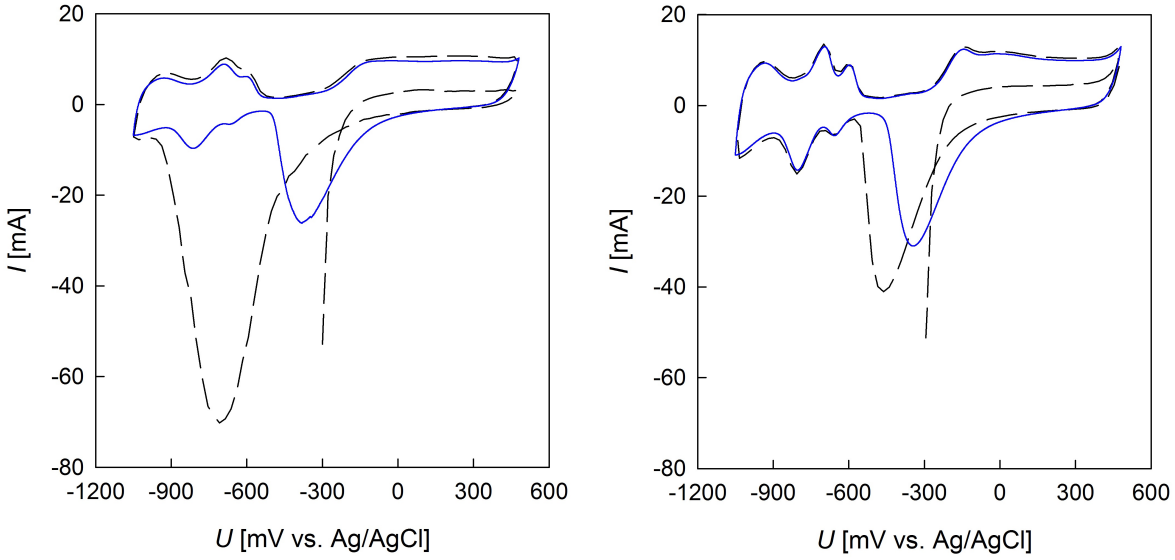

(a) np-Pt300-2 **(b)** Pt-pellet 2

Figure 3.12: Comparison of the cyclic voltammograms recorded with a scan rate of $v = 0.5\,\mathrm{mV/s}$ for (a) np-Pt300-2 prepared by dealloying and (b) Pt-pellet 2 prepared by powder compaction. The blue solid line represents the fourth CV cycle, whereas the black dashed line corresponds to the first cycle. The dominant negative peak in the cathodic part of the first cycle originates from oxygen desorption. In the case of the dealloyed sample (a), the oxygen desorption peak is more pronounced (bigger charge) and is desorbed at more negative potentials as compared to the Pt-pellet.

The dashed lines correspond to the first of four cycles, being significantly different than the last. In this first cycle, the oxygen desorption peak is rather pronounced for the dealloyed sample. This indicates that a significant amount of oxygen atoms must be present due

to the dealloying at positive potentials. Furthermore, this peak is shifted towards a more negative potential than in the following cycles. This effect is again particularly strong for the samples fabricated via dealloying where the O-desorption peak position in the first cycle is located at -750 mV. For the Pt-pellets, it is located at -465 mV. This phenomenon was described for Pt by Angerstein et al. [38]. They conducted potential hold experiments for various times and potentials at the end of an anodic sweep (positive potentials) and subsequently continued with a cathodic sweep. It was shown that the oxide reduction peak moved to more negative potentials with increasing time held at a respective potential at the end of an anodic sweep. This was explained by an oxygen rearrangement effect, resulting in O and Pt exchange processes, leading to a more stable oxide layer.
In the case of dealloying, the additional rearrangement of Pt atoms due to surface diffusion will therefore very likely lead to oxygen atoms existing even deeper in the ligaments, and not just a surface oxide layer with some oxygen atoms below the surface. In fact, as assumed in Section 3.2.1, each Pt atom will adsorb one O^{2-} ion during the dealloying process, which was in close agreement with the experimentally obtained charges via dealloying (see Section 3.3). Furthermore, estimating the charge attributed to the oxygen desorption peak of the cyclic voltammogram for np-Pt300-2, yields $Q_{O,desorption} = 40.94\,\mathrm{As}$. Comparing this value to the charge that would result from an O^{2-} adsorption per each Pt-atom of this sample, i.e., $Q_{expected} = 44.49\,\mathrm{As}$ [7], shows a 92 % agreement. We therefore believe that the dealloying process does not only lead to a strongly bonded surface oxide, but rather to PtO ligaments.

In case of the Pt samples prepared by powder compaction (Figure 3.12b), the oxide is just superficial and is therefore more easily dissolved as compared to the dealloyed samples. Furthermore, the oxide reduction peak is smaller even though the pellets exhibit a larger total surface area (compare Table 3.4). This indicates, that there is only a very thin oxide layer present, resulting from the storage of the powder under ambient atmosphere. Note that due to the smaller sample size and the reduced thicknesses, the dealloyed samples exhibit a smaller total surface area compared to the pellets. Thus, the currents observed in the cyclic voltammogram are lower for the dealloyed sample (Figure 3.12a).

After recording the CVs, the samples were rinsed with and stored in distilled water for several hours. After drying over night, the sample masses were determined to calculate the specific surface. The resulting specific surface areas that were derived from the last cycle, are listed in Table 3.4 and 3.5 for the surfaces after oxide reduction and after annealing,

[7] The number of Pt-atoms in this sample (mass listed in Table 3.3) was calculated from the number of atoms in 1 g $Cu_{75}Pt_{25}$ derived in Section 3.2.1, and multiplied by 2e.

respectively.

Table 3.4: Surface areas determined from cyclic voltammetry measurements (10 % uncertainty). The specific surface areas were calculated according to (3.7) and are to be understood as specific surface areas after oxide reduction.

	np-Pt180		**np-Pt300**		**Pt-pellets**	
	1	**2**	**1**	**2**	**1**	**2**
Mass [mg]	23.78	20.29	59.24	48.63	163.90	167.81
$\mathbf{Q}_H$ [As]	1.6380	1.4842	4.8952	4.0666	5.8436	5.8582
Surface area [cm^2]	7800	7067	23310	19365	27826	27896
Specific surface area [m^2/g]	32.8	34.8	39.3	39.8	17.0	16.6

Table 3.5: Surface areas determined from cyclic voltammetry measurements after annealing at 500 °C (10 % uncertainty). The specific surface areas were calculated according to (3.7).

	np-Pt300		**Pt-pellets**	
	1	**2**	**1**	**2**
Mass [mg]	36.96	34.17	142.14	163.25
$\mathbf{Q}_H$ [As]	0.3261	0.6495	0.2792	0.3814
Surface area [cm^2]	1553	3093	1330	1816
Specific surface area [m^2/g]	4.2	3.3	0.9	1.1

CHAPTER 4

Fast-Fast Positron Lifetime Spectrometer

To measure positron lifetimes, a fast-fast positron lifetime spectrometer was used during this work. Figure 4.1 schematically depicts the block diagram of such a lifetime spectrometer. The different blocks are normed modules. This means that the connectors, power supply, size etc. are normed according to the nuclear instrumentation module Standard (NIM). This building block principle has the advantage of being able to easily exchange defect modules and realize many different experiments. The connections between these are established by 50 Ω BNC cables.

4.1 Functional Principle

The setup consists of two photomultipliers (PM), one to detect the 1275 keV start quantum, and another one to detect one of the collinearly emitted 511 keV stop quanta. The principal goal is now to measure the time difference between many of these two events. Since the photocathode of the photomultiplier is working only for visible light, a scintillator is attached to the photocathode. This scintillator transforms the gamma rays, which are emitted during the birth and the annihilation of the positrons, to flashes of visible light which can then in turn generate electrons at the photocathode. These are accelerated along the dynode stages of the photomultiplier and result in an energy-proportional pulse at the anode output.
This pulse is forwarded to the constant fraction differential discriminator (CFDD), which executes two tasks. First, it imposes an energy window onto the signal. Only if the pulse energy ranges between a lower and an upper limit of a defined energy window (corresponding

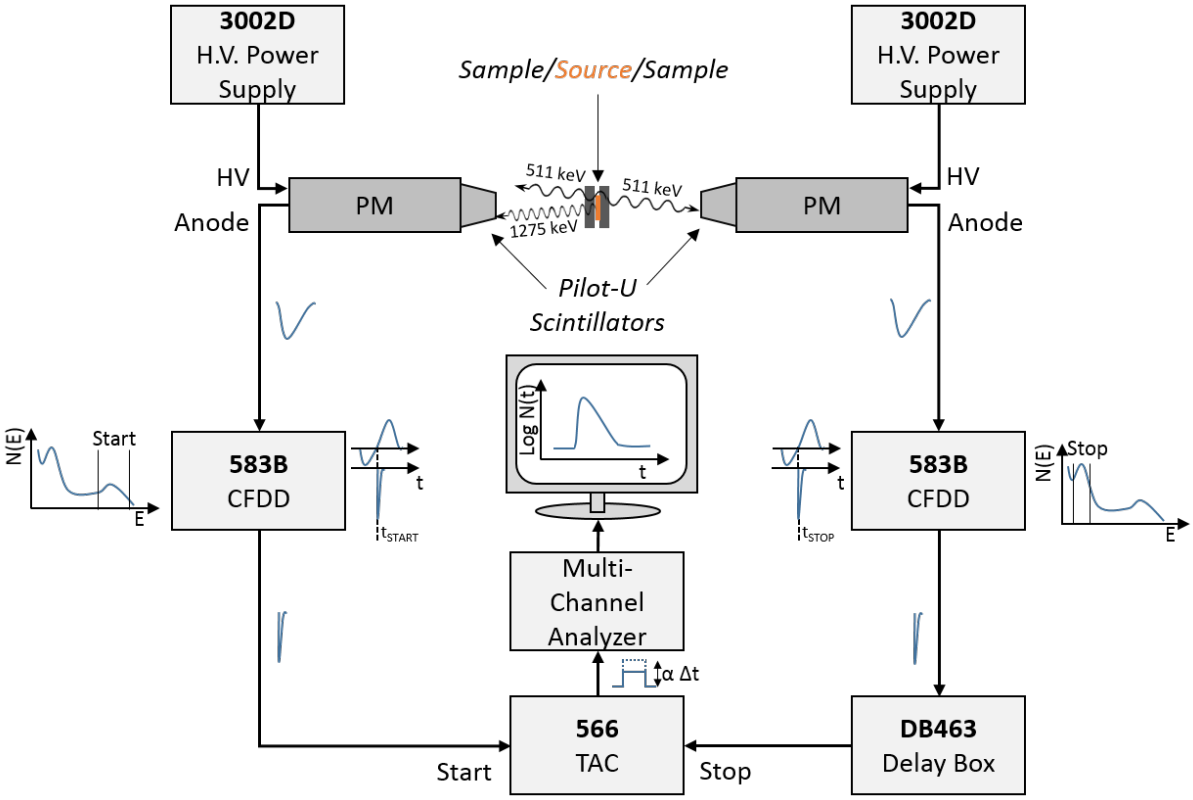

Figure 4.1: Block diagram of the fast-fast lifetime spectrometer. The pulse forms are displayed in blue next to the cables. The start branch is depicted at the left side of the diagram.

H.V. Power Supply ..... Canberra 3002D
PM ..... Hamamatsu H2431-50 photomultipliers
CFDD ..... Constant fraction differential discriminator, ORTEC 583B
Delay Box ..... ORTEC DB463
TAC ..... Time-to-amplitude converter, ORTEC 566

to the start quantum or stop quantum energy, respectively), this pulse is processed in a second step. The CFDD now delivers a narrow timing pulse at the arrival time of the input pulse. This is done by internally shaping the anode signal such that it exhibits a zero-crossing almost independent of the energy-proportional pulse height. This is the so-called constant fraction discrimination. The output of the CFDD is a narrow timing pulse at the time of the zero-crossing.

The two fast CFDD output signals, one originating from the start quantum, the other one from the stop quantum, are delivered to a time-to-amplitude-converter (TAC) which generates a signal with a height proportional to the time difference between these two signals. In order to avoid the problem of a potentially slower working stop CFDD[8] and to force the TAC to operate in its most linear regime, the stop output of the CFDD is delayed by several ns. The TAC waits an adjustable time range for the stop signal to appear after the start signal. This time difference is then stored in the corresponding channel of a multi-channel-analyzer (MCA). It is important to note that the measured time differences are not yet the different positron lifetimes. This is a result of different signal processing times of different modules, different cable lengths, electronic instabilities and the artificial delay imposed on the stop pulse. The recorded histogram of number of events per time channel has to be mathematically analyzed in a subsequent step in order to calculate the positron lifetimes.

4.2 Mounting in Sandwich Geometry

The sandwich consists of two as far as possible identical samples with the foil source placed in between. During this work, the sample sandwiches were placed horizontally onto a sample holder between the detectors. In order to maximize the count rate, a sample holder as small as possible was fabricated (10 mm wide, see Figure 4.2a). As the count rate scales quadratically with the distance, halving the source-detector distance leads to an increase in count rate by a factor of four (distance law).

Because of the small dimensions of the dealloyed samples ($6 \times 6\,\mathrm{mm}^2$) and the slightly curved surface, it is possible that a small fraction of positrons escapes the sandwich and does not annihilate within the sample. This could be for instance the sample holder, giving rise to an unknown lifetime contribution. In order to avoid unknown, possibly long-lived lifetime

[8] This could implicate that the stop pulse arrives at the TAC before the start pulse. In this case, no valid count is collected.

components from surroundings, two copper boxes were fabricated from a 99.9985 % purity 100 μm thick copper foil. If now a small fraction of positrons escape the sandwich, they will annihilate in copper, which has a short lifetime of 110 ps [39]. Measuring our samples in a copper box thus makes sure that measured long lifetimes really originate from the sample. Figure 4.2b shows the Cu-box made for the new sample holder. In order to anneal-out defects that were generated during the fabrication, the boxes were annealed for 8 h in a vacuum furnace at $T = 600\,^{\circ}\mathrm{C}$ ($p \approx 2.5 \cdot 10^{-6}$ mbar).

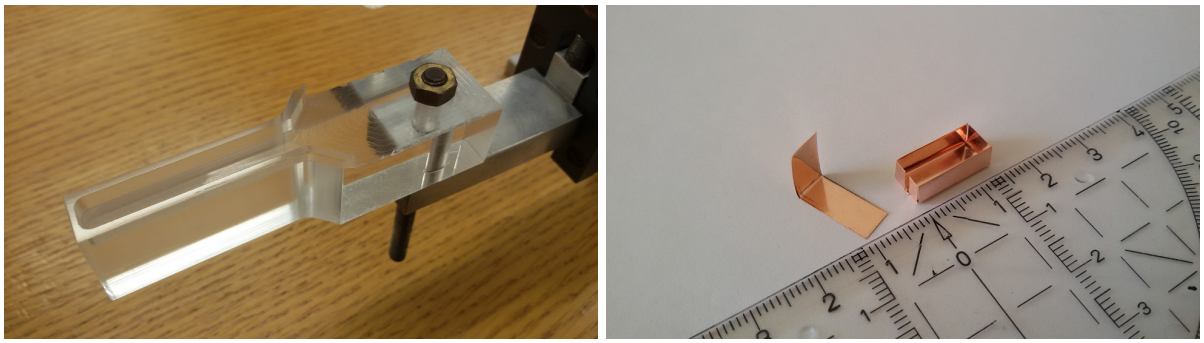

(a) **(b)**

Figure 4.2: (a) A small sample holder was fabricated in order to maximize the count rate for samples as broad as 6 mm. (b) The fabricated copper box (with lid) that fits into the manufactured sample holder.

4.3 Measurements under Vacuum Condition

During this work, the positron lifetime measuring setup was also equipped with a vacuum pumping station (Pfeiffer Vacuum).

As depicted in Figure 4.3, a glass tube was used as sample holder. To eliminate the risk of the radioactive source being sucked into the pump, a fine-meshed metal net was placed between metal pipe and glass tube. For lifetime measurements with the dealloyed samples, the source/sample sandwich was simply put into the fabricated copper box and then moved to the end of the glass tube. Because of the bigger size of the Pt-pellet sandwich (8 mm diameter in the as-prepared state), this sandwich had to be wrapped into aluminum foil and was inserted vertically into the tube.

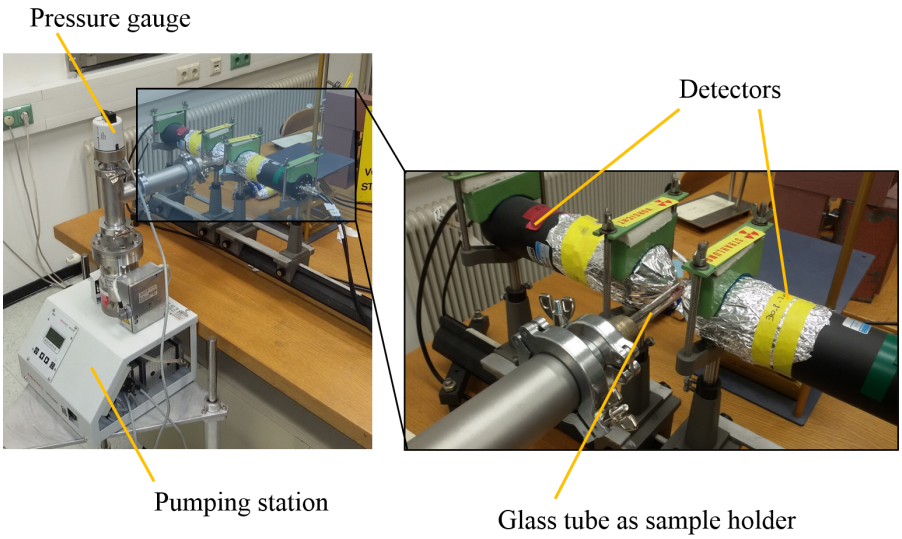

Figure 4.3: Measurement setup for positron lifetime measurements under vacuum condition.

4.4 Time Scale of the Spectrometer

As was previously explained, the annihilation events are stored in the channels of an MCA. Without knowing the time per channel (time scale), no lifetimes can be determined from the spectra.

The time scales were determined by recording half-hour spectra with increasing stop-pulse delays. Doing so, the spectra are shifted to higher channel numbers. Afterwards, the first momenta are determined with the program `2_MOMENT.exe` (see Appendix) and the delays are plotted as a function of these first momenta (see Figure 4.4). The slope of the resulting straight line yields the time scale with the unit $^{\text{ns}}/_{\text{channel}}$ and is determined via a linear regression. Table 4.1 collates the delays and the corresponding first momenta for an MCA conversion gain of 4096 and 2048 channels, respectively.

Table 4.1: First momenta as a function of the stop-delay to determine the time scale for MCA conversion gains of 4096 and 2048 channels with a TAC time range of 50 ns.

Delay [ns]	4096 channels **1st momentum**	2048 channels **1st momentum**
4	454.07800	226.82802
8	786.85101	393.25626
12	1112.15710	555.62329
16	1451.10425	725.06757
32	-	1384.79333

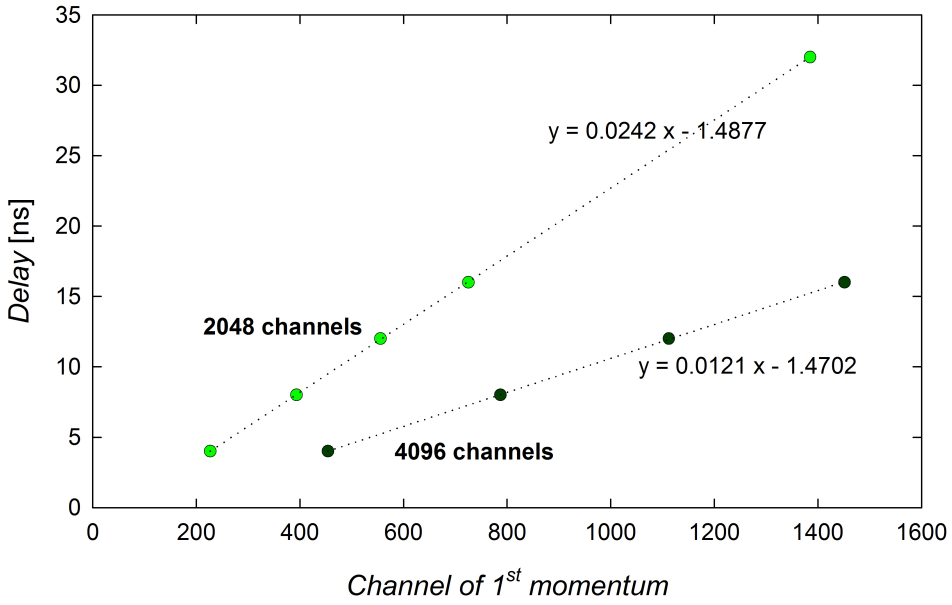

Figure 4.4: Stop-delays as a function of the respective first momenta and linear regression for time scale determination for an MCA conversion gain of 4096 channels (black circles) and 2048 channels (green circles). The TAC time range is 50 ns.

The determined time scales are 12.1 $^{\text{ps}}/_{\text{channel}}$ for a conversion gain of 4096 channels, and twice this value for 2048 channels, i.e., 24.2 $^{\text{ps}}/_{\text{channel}}$.

4.5 Resolution Function of the Spectrometer

As was described in Section 2.3.1, the resolution function of the spectrometer has to be determined to deconvolve the measured spectra. To obtain this function, a reference sample with a well-defined single lifetime is measured. Additionally, a longer lifetime with low intensity can be determined which results from the positron source (NaCl-crystals + Al-foil).

For further lifetime measurements at more complex materials, this very source component can then be subtracted form the spectra and thus reveal the positron lifetimes belonging to the sample only. In this work, we used defect-free Si as reference sample. The bulk lifetime, that should result from a free fit (i.e., no lifetimes fixed) within a few ps, is $\tau_{Si} = 218$ ps [40]. The resolution fits were conducted in PALS*fit*. Typically, a sum of three Gaussians with the intensities 15/70/15 turned out to be a good choice and two-term fits were conducted.

The resolution function can be characterized by the FWHM of the resulting Gaussian (see

Section 2.3.1). Table 4.2 shows the lifetimes of source and Si, respectively, as well as intensities and FWHM values for the different resolution functions. As can be seen, the spectrometer shows a rather constant FWHM of 241.5 to 245.8 ps.

Table 4.2: Resolution function measurements with Si samples. The upper line entries in the multi-rows correspond to Si, while the lower lines describe the source correction. Except for the first resolution function, the stronger source L1 was used.

No.	τ_{Si}/τ_Q [ps]	I_{Si}/I_Q [%]	var	counts [10^6]	FWHM [ps]	Note
1	217.6±1.0 563.8±44.8	98.5±0.3 1.5±0.3	1.180	1.2	241.5	ambient atmosphere
2	216.1±1.4 494.3±20.0	94.7±0.7 5.3±0.7	1.182	1.8	245.4	ambient atmosphere
3	219.8±0.8 544.7±14.8	96.0±0.3 4.0±0.3	1.285	4.3	245.8	ambient atmosphere
4	223.4±0.3 892.3±19.5	98.2±0.1 1.8±0.1	1.564	5.1	243.5	vacuum
5	216.9±0.7 545.5±14.5	96.0±0.3 4.0±0.3	1.327	3.9	244.2	ambient atmosphere in pumping station
6	222.0±0.4 828.3±17.9	98.0±0.1 2.0±0.1	1.644	5.0	243.5	vacuum

CHAPTER 5

Positron Lifetime Results

In this chapter, the measured positron lifetime spectra of the nanoporous Pt samples and the resulting lifetimes and intensities that were extracted using the program PALS*fit*, are presented.

If not stated otherwise, 30 min spectra were recorded and summed up to a spectrum of approximately $3 \cdot 10^6$ counts. For measurements with an MCA-conversion gain of 4096 channels (12.1 $^{\text{ps}}/_{\text{channel}}$), only spectra with the first momenta within one channel width were considered. The background per channel values were obtained from channels higher than 1500, which corresponds to $t > 18.15$ ns. For data acquisition with an MCA conversion gain of 2048 channels (24.2 $^{\text{ps}}/_{\text{channel}}$), only spectra with the first momenta within half a channel width were processed. In the latter case, the background per channel was calculated from channels higher than 1250, i.e., $t > 30.25$ ns. The first channel for background determination was at the same time chosen as the last channel of the fit interval.

For measurements under vacuum condition only spectra were considered after the pressure p dropped below 10^{-6} mbar. For the sake of easier comparison, all spectra were peak-normalized before plotting.

Figures 5.1a, 5.1b and 5.1c show how the samples were treated before lifetime measurements were conducted. Each arrow represents a lifetime measurement, where blue arrows correspond to measurements under ambient atmosphere while green arrows represent measurements in vacuum.

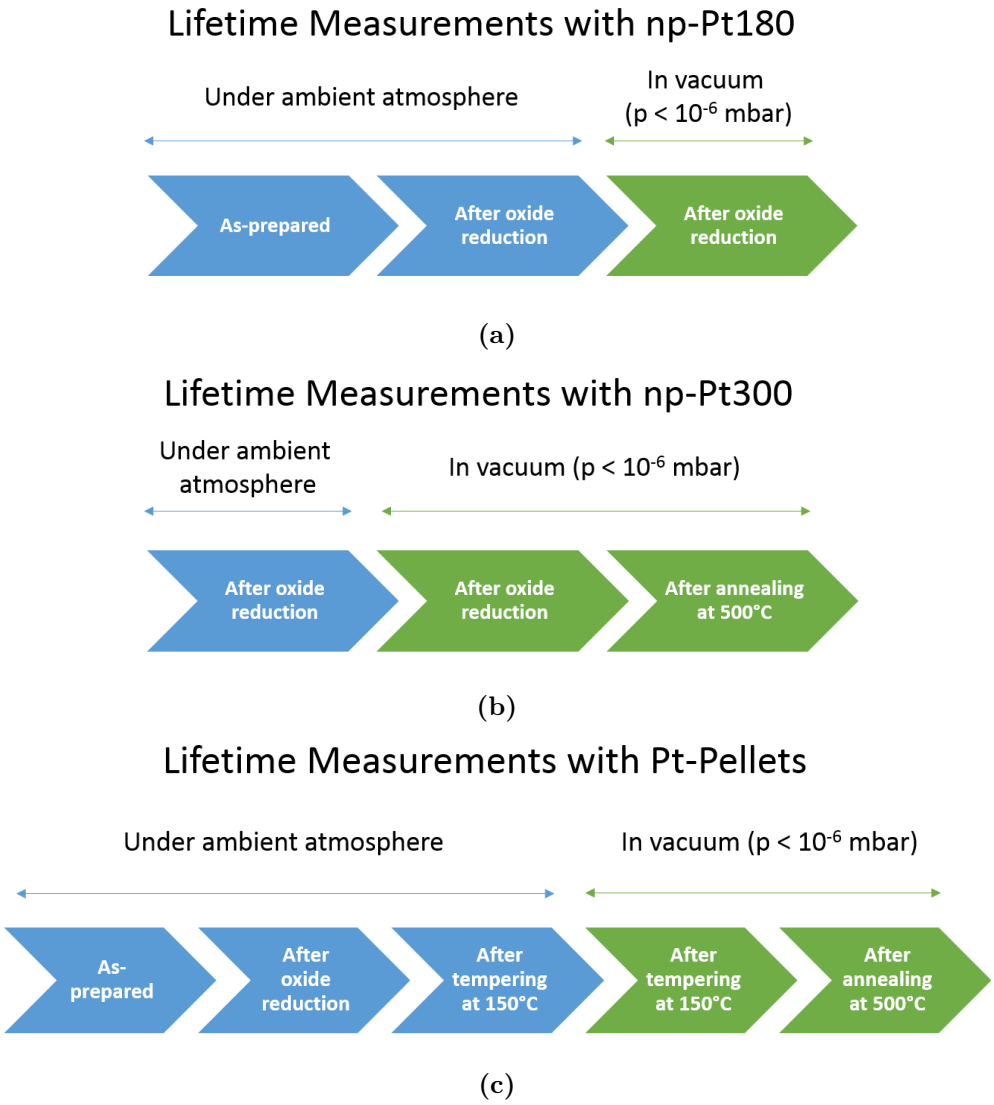

Figure 5.1: Work flow for positron lifetime measurements conducted with the (a) np-Pt180, (b) np-Pt300 and (c) Pt-Pellet samples. Blue arrows represent lifetime measurements under ambient atmosphere, while green arrows correspond to measurements conducted in vacuum.

5.1 Ps Formation in Teflon

In order to set up the spectrometer for the measurement of long lifetime components in the nanosecond regime, the channel number and channel width of the ADC/MCA combination has to be set accordingly. Therefore, a Teflon sample was used for which positronium formation is known. The spectrum was cumulatively recorded with a number of $1.8 \cdot 10^6$ counts and is depicted in Figure 5.2. The free four-component analysis yielded a variance of 1.116, the received lifetimes and intensities are summarized in Table 5.1.

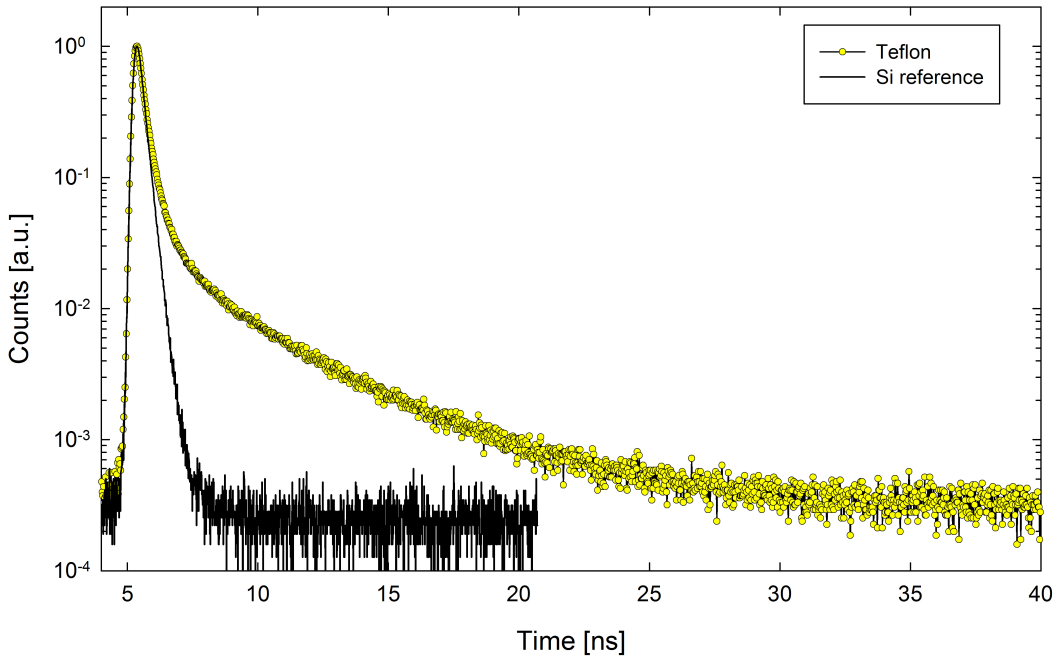

Figure 5.2: Peak-normalized positron lifetime spectrum of Teflon (yellow circles). A Si spectrum is depicted as reference (black solid line). The Teflon spectrum clearly shows long-lived annihilation events.

Table 5.1: Positron lifetimes and intensities in Teflon. The measurement confirms that the spectrometer can detect lifetimes in the ns region.

τ [ps]	I [%]
152±6	30.6±3.0
321±11	45.8±2.6
1220±60	9.8±0.4
4190±40	13.8±0.2

As was previously described by Kindl et al. for γ-irradiated Teflon, four lifetime components

can be extracted [41]. Among these, two long-lived annihilation events are present where the longest one with $\tau_4 \approx 4.2\,\text{ns}$ can be attributed to o-Ps pick-off annihilation.
The existence of these long-lived components in the recorded spectrum demonstrated that the spectrometer settings are suitable for the investigation of the nanoporous samples. It should however be noted that the mechanism leading to Ps formation in Teflon, and generally in molecular substances, is a different one than for metals.

5.2 Positron Lifetime Measurements with np-Pt180

Figure 5.3 shows the recorded spectra for the samples np-Pt180. In order to be able to put the measured spectra into context, a Si-reference spectrum is plotted together with the data for the nanoporous samples. Table 5.2 lists the obtained lifetimes and intensities as well as the variance of the fits. Furthermore, the mean lifetimes were calculated according to (2.29) and are listed in this table. The behaviour of the individual lifetimes and intensities is graphically depicted in Figure 5.4.

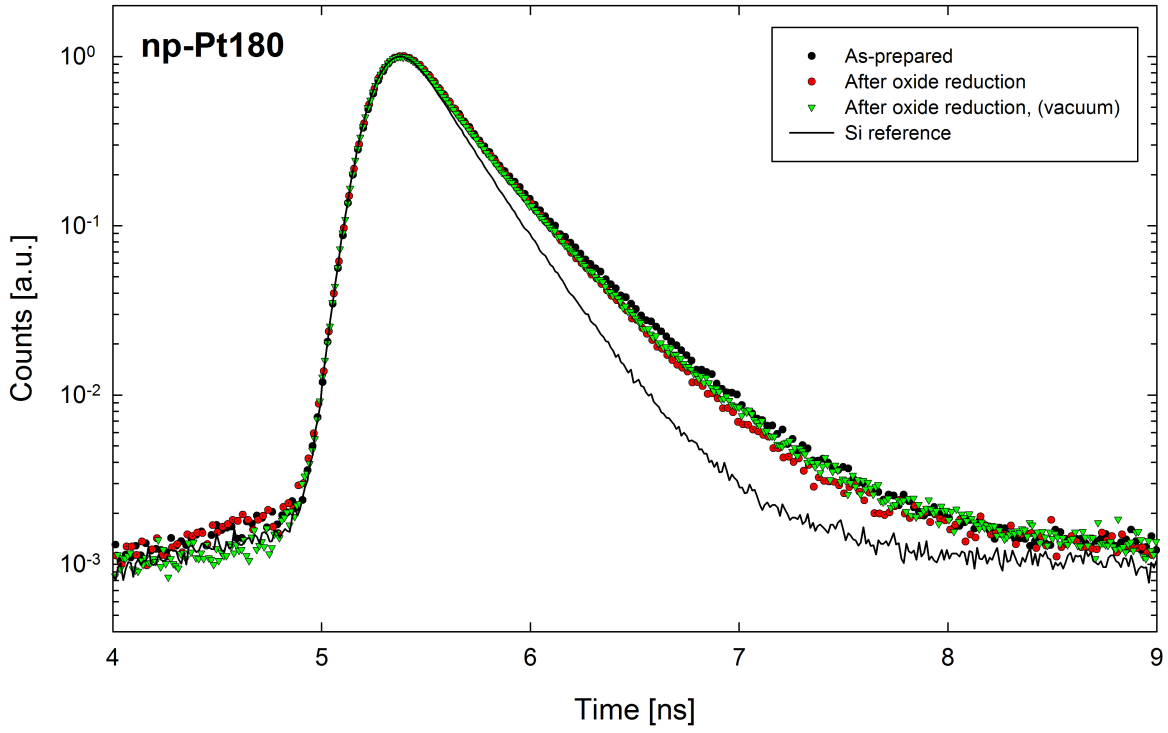

Figure 5.3: Peak-normalized positron lifetime spectra for the sample np-Pt180 after different treatments. A Si-spectrum is depicted as reference (black solid line).

Table 5.2: Sample np-Pt180: Measured lifetimes τ and intensities I as well as mean lifetime τ_m derived from free three-term fits (var = variance of the fit). If not stated otherwise, the measurements were conducted under ambient atmosphere.

	np-Pt180			
	τ [ps]	I [%]	τ_m [ps]	*var*
As-prepared	177±4	38.07±2.23	288.2	1.043
	344±4	61.42±2.18		
	1820±220	0.51±0.08		
After oxide reduction	169±8	27.41±3.68	274.6	1.111
	302±4	72.00±3.64		
	1840±190	0.59±0.07		
After oxide reduction (Vacuum)	188±4	40.39±1.99	294.1	1.126
	339±3	59.21±1.98		
	4360±380	0.40±0.02		

As-prepared

The black circles in Figure 5.3 correspond to the as-prepared, i.e., as-dealloyed samples. The spectrum was cumulatively recorded with a total number of $2.2 \cdot 10^6$ counts. In this state, PtO ligaments are believed to be present due to the dealloying process (compare Section 3.4). Evaluating the spectrum with a free, three-component analysis, yielded a lifetime component of 177 ps with $I_1 \approx 38\,\%$ and a second component with 344 ps, $I_2 \approx 61\,\%$. Furthermore, a long-lived annihilation event with about 1.8 ns lifetime and 0.5 % is present in the spectrum. The mean lifetime attributed to this spectrum is $\tau_m = 288.2$ ps. Because of the small intensity of τ_3, it was assumed that the oxide perturbs Ps formation by hindering the positrons to be ejected into the pores. Consequently, the next step in trying to enhance Ps formation was to electrochemically reduce the oxide (see Section 3.4).

After oxide reduction

The red dotted circles in Figure 5.3 represent the lifetime spectrum recorded after the oxide was reduced. The spectrum was again cumulatively recorded with a number of $1.8 \cdot 10^6$ counts. The long component is still present but neither lifetime, nor intensity changed significantly. Furthermore, the components τ_1 and τ_2 both decreased with respect to the lifetimes measured in the as-prepared state, where τ_1 is now 169 ps and $\tau_2 = 302$ ps, with τ_2 being the dominant lifetime in the spectrum ($I_2 = 72\,\%$). Compared to the measurements conducted with the as-prepared samples, the mean lifetime declines to 274.6 ps.

After oxide reduction, measured in vacuum

To avoid the effect of adsorbed gases, work on positronium formation at metal surfaces should be conducted in vacuum. The resulting spectrum obtained under vacuum condition

is marked with green triangles in Figure 5.3. As before, judging from the variance, a three-term fit was needed to describe the underlying physics. The intensity of the long lifetime component τ_3 decreases slightly, while the lifetime itself increases to 4.4 ns, which is more than twice than what was measured under ambient atmosphere. Also the lifetimes τ_1 and τ_2 increase to 188 ps and 339 ps, respectively, while the difference in intensities decreases ($I_1 \approx 40\,\%$ and $I_2 \approx 59\,\%$). Furthermore, a mean-lifetime increase of about 20 ps can be observed ($\tau_m = 294.1$ ps).

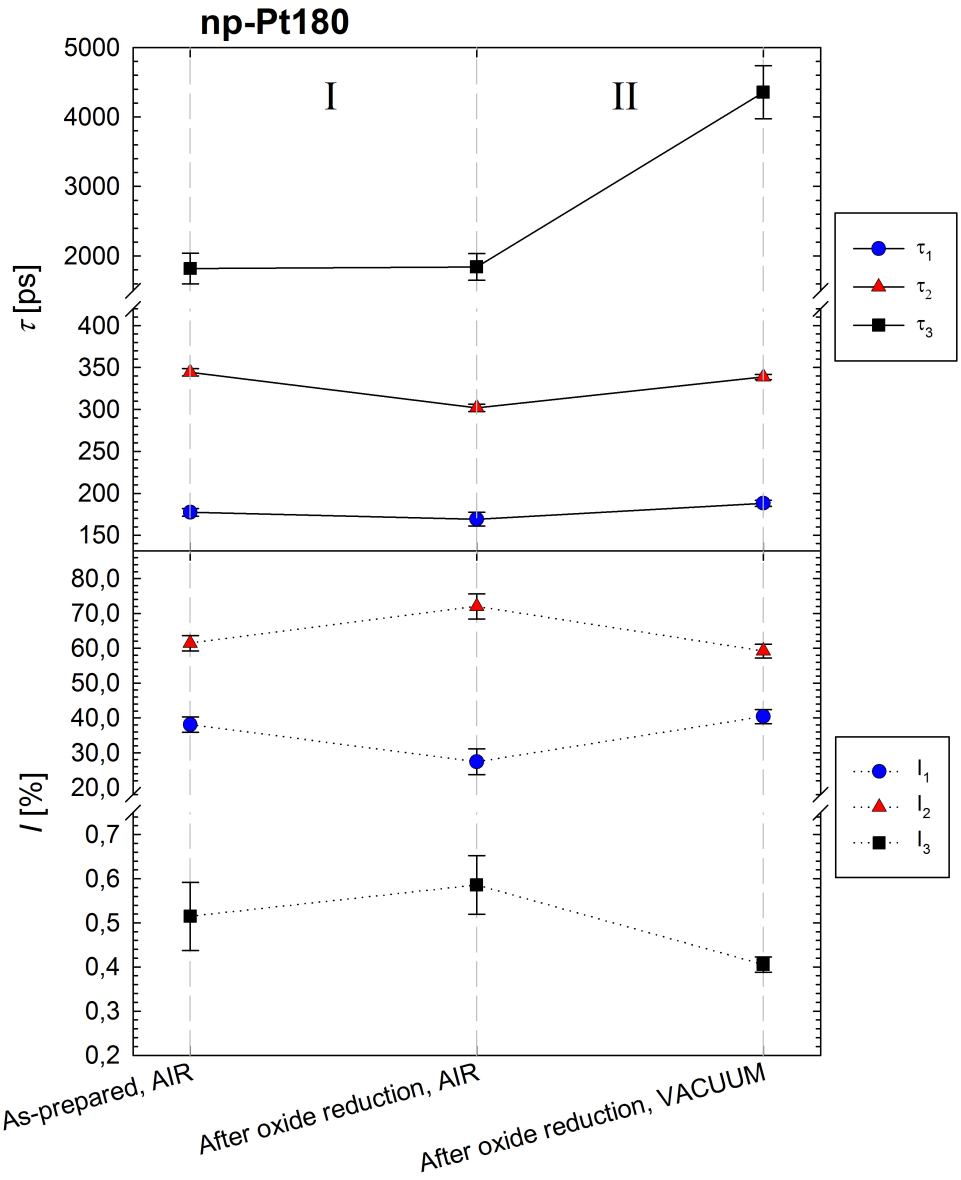

Figure 5.4: Obtained lifetimes and corresponding intensities for different treatments of the np-Pt180 samples.

5.3 Positron Lifetime Measurements with np-Pt300

In Figure 5.5, the recorded spectra of the samples np-Pt300 are depicted. A Si-reference spectrum is plotted together with the data for the nanoporous samples. Additionally, the $Cu_{75}Pt_{25}$ alloy was subjected to a lifetime measurement and the corresponding spectrum is also plotted in Figure 5.5. Table 5.2 lists the obtained lifetimes and intensities as well as the variance of the respective fits. The mean lifetimes that were calculated according to (2.29) are also listed in this Table. Figure 5.6 shows the evolution of the lifetimes and intensities for the different measurements.

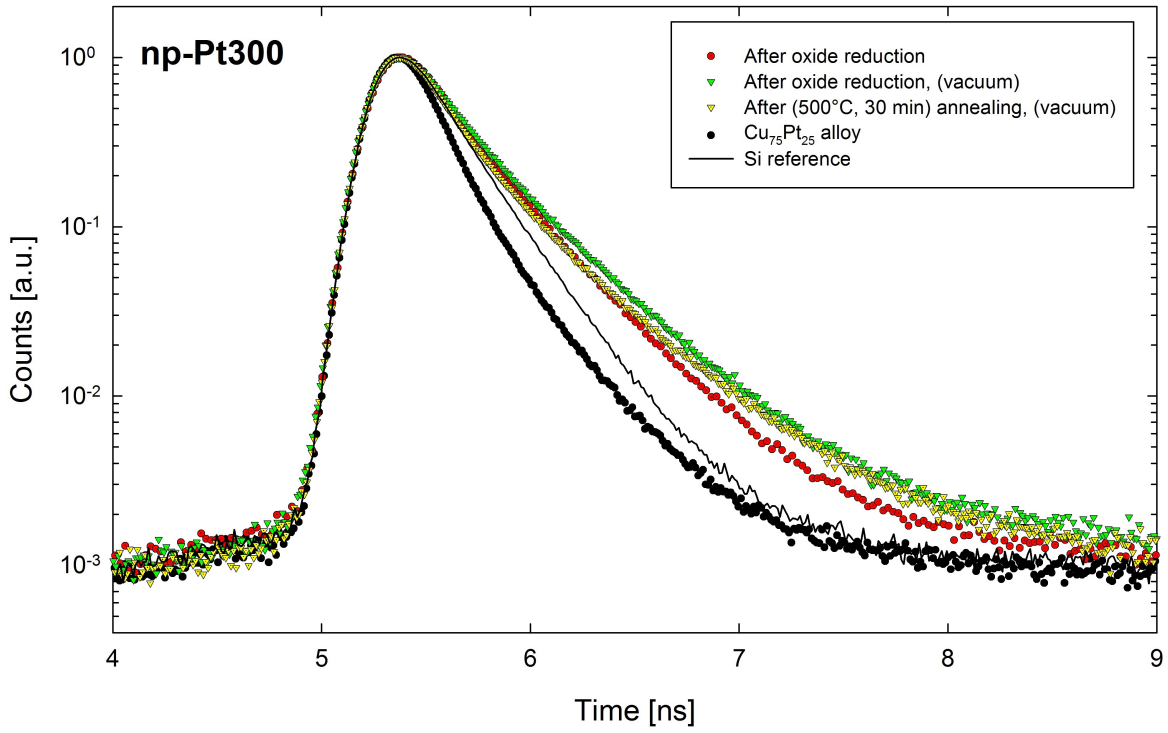

Figure 5.5: Peak-normalized positron lifetime spectra for the sample np-Pt300 after different treatments as well as the master alloy $Cu_{75}Pt_{25}$. A Si-spectrum is depicted as reference (black solid line).

Table 5.3: Sample np-Pt300: Measured lifetimes τ and intensities I as well as mean lifetime τ_m derived from free three-term fits (var = variance of the fit). If not stated otherwise, the measurements were conducted under ambient atmosphere.

	np-Pt300			
	τ [ps]	I [%]	τ_m [ps]	*var*
$Cu_{75}Pt_{25}$ alloy	124±1	65.0±1.2	165.6	1.563
	242±2	35.0±1.2		
After oxide reduction	172±5	32.27±2.28	276.1	1.205
	315±3	67.35±2.26		
	2180±390	0.38±0.04		
After oxide reduction (Vacuum)	193±3	40.45±1.48	314.0	1.127
	377±3	59.11±1.46		
	2960±270	0.44±0.03		
After annealing at 500 °C (Vacuum)	173±2	53.11±0.76	286.5	0.986
	394±3	46.61±0.75		
	3700±490	0.28±0.02		

$Cu_{75}Pt_{25}$ alloy

The black circles in Figure 5.5 represent the spectrum measured for the cut and cleaned master alloy samples in the as-received state before dealloying. This spectrum was recorded cumulatively and is composed out of $4 \cdot 10^6$ counts. Two components appear in the analysis, a short τ_1 with 124 ps, $I_1 = 65\,\%$ and a longer one with $\tau_2 = 242$ ps. The mean lifetime calculated from the obtained lifetimes and intensities is 165.6 ps.

After oxide reduction

Since the samples np-Pt180 yielded no high contribution of the long lifetime component in the as-prepared state, no positron lifetime measurement was conducted with np-Pt300 in this state. Instead, the oxide was reduced right after dealloying. The red dotted circles in Figure 5.5 show the resulting spectrum after oxide reduction. A three component analysis of the spectrum yielded $\tau_1 = 172$ ps with an intensity of $I_1 \approx 32\,\%$, while the second component, $\tau_2 = 315$ ps and $I_2 = 67\,\%$, is the dominant one. As was also observed after oxide reduction for the np-Pt180 specimens, a long lifetime component is obtained in the analysis and results in $\tau_3 = 2.2$ ns with an intensity of 0.38 %. The mean lifetime of 276.1 ps is identical to the one obtained for the np-Pt180 samples.

After oxide reduction, measured in vacuum

Measuring the very same samples in vacuum, an increase in both τ_1 and τ_2 with respect to the measurement under ambient atmosphere can be observed. The related spectrum is depicted with green triangles in Figure 5.5. While τ_1 and τ_2 increase to 193 ps and 377 ps,

respectively, the difference between the corresponding intensities decreases, resulting in $I_1 \approx 40\,\%$ and $I_2 \approx 59\,\%$. An increased long-lived lifetime component with $\tau_3 \approx 3\,\text{ns}$ and an intensity of 0.44 % is again present in the spectrum. The mean lifetime attributed to this measurement increased by 38 ps as compared to the measurement under ambient atmosphere, and yields 314 ps.

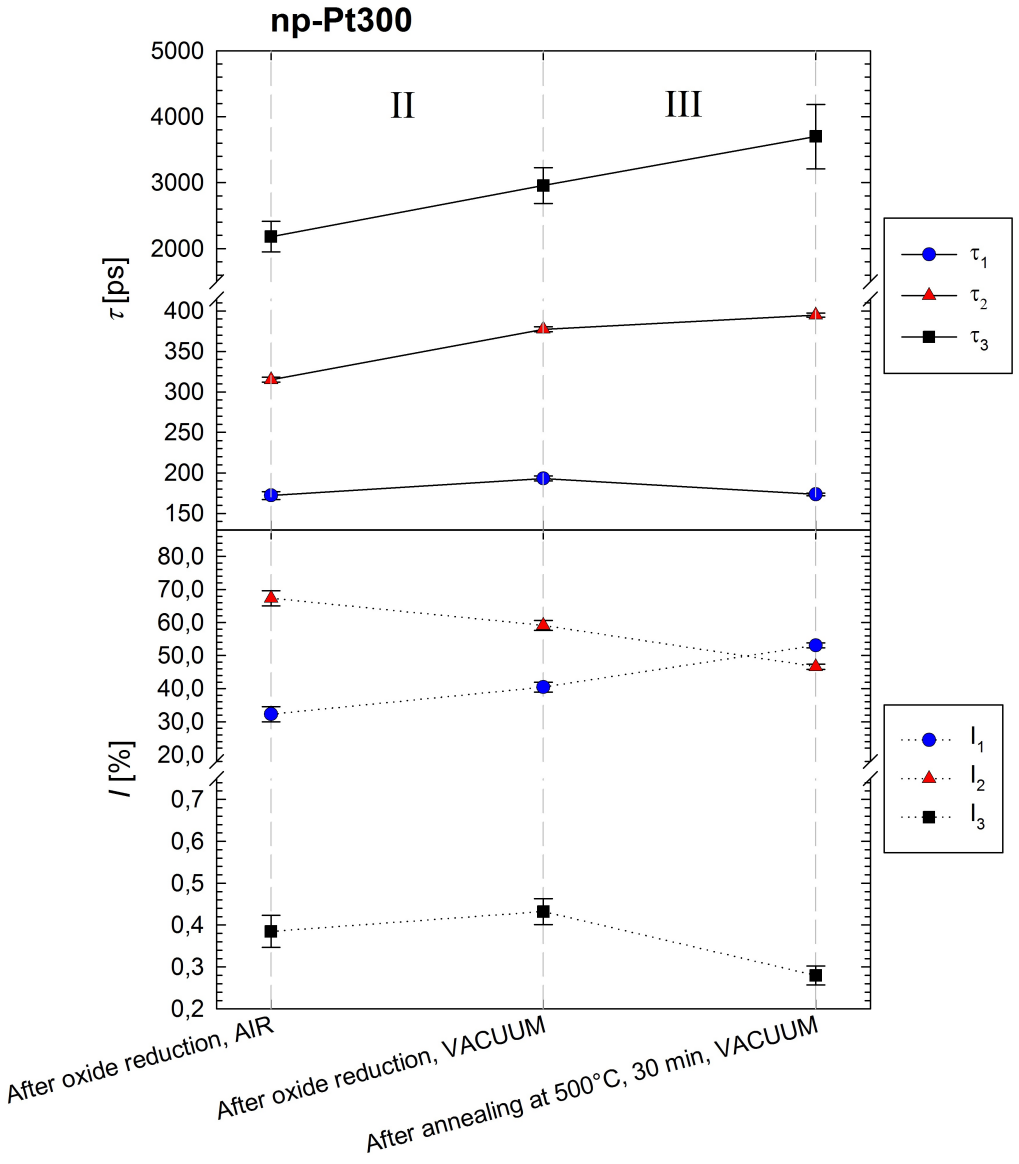

Figure 5.6: Obtained lifetimes and corresponding intensities for different treatments of the np-Pt300 samples.

After annealing at 500 °C for 30 min, measured in vacuum

In positron lifetime studies of np-Au done by Viswanath et al., a third lifetime with $\tau \approx 600\,\text{ps}$ and $I \approx 6\,\%$ developed in the spectrum, after the samples were annealed at

600 °C for 6 h [13]. This heat-treatment led to coarsening of the pores and ultimately to a closed pore structure while the vacancies were annealed out. This newly developed third component was explained by pick-off annihilation of positronium that formed inside voids and pores. To investigate the evolution of lifetimes in the np-Pt sample after annealing-out of possible vacancies and coarsening of the pores, the samples were therefore heat-treated. The experimental procedure is described in Section 3.2.6.
In this step, the short lifetime decreases by 20 ns ($\tau_1 = 173$ ps) and becomes the dominant lifetime with 53 %, while the second lifetime increases by 17 ps (394 ps) with $I_2 \approx 47$ %. The long lifetime τ_3 rises to 3.7 ns, but remains within error of the last measurement. The corresponding intensity decreases to 0.28 %. Because of the now dominant lifetime τ_1 and the declined intensity I_3, the mean lifetime also decreases again ($\tau_m = 286.5$ ps).

5.4 Positron Lifetime Measurements with Pt-Pellets

In Figure 5.7, the positron lifetime spectra for the Pt-pellets are shown. Together with the spectra representing the pellets after different treatments, a Si-reference spectrum is plotted for comparison. Table 5.4 lists the received lifetimes, intensities, calculated mean lifetimes according to (2.29) as well as the variance of the conducted fits. The evolution of lifetimes and intensities is depicted in Figure 5.8.

As-prepared

The spectrum recorded for the Pt-pellets in the as-prepared state is marked with black circles in Figure 5.7. The lifetime analysis yielded three components, being $\tau_1 = 198$ ps, $\tau_2 = 345$ ps and a long lifetime of 2.1 ns with an intensity of 0.39 %. The intensities of the shorter lifetime components are $I_1 \approx 45$ % and $I_2 \approx 55$ %, respectively. The calculated mean lifetime of 286.5 ps is in close correspondence with the np-Pt180 samples in the as-prepared state.

After oxide reduction

While the short lifetime remains constant ($\tau_1 = 195$ ps), electrochemically reducing the surface oxide leads to a decrease in τ_2 to a value of 319 ps, while the long component increases slightly to a value of 2.3 ns with an intensity declining to 0.28 %. This increase in τ_3 is however within the error margin of the long lifetime as measured in the as-prepared state. As was also observed with the np-Pt180 as well as the np-Pt300 samples, the intensities of τ_1 and τ_2 tend to spread farther apart after oxide reduction, here $I_1 \approx 39$ % and $I_2 \approx 61$ %. The

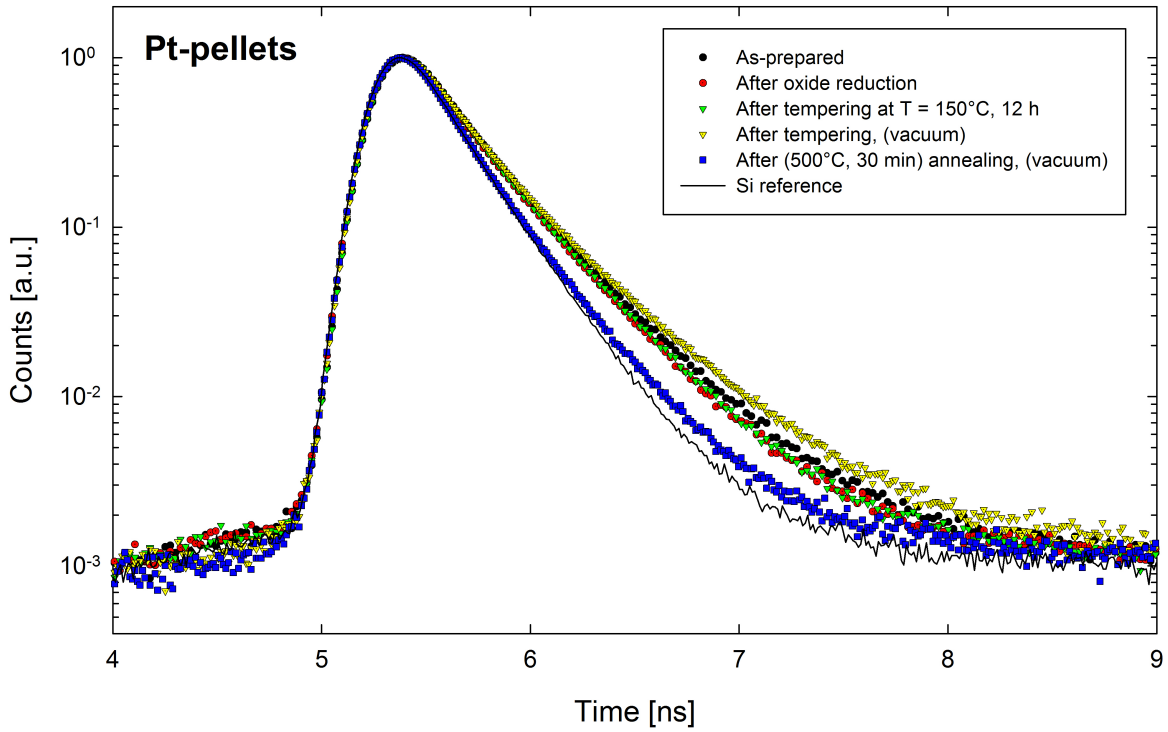

Figure 5.7: Peak-normalized positron lifetime spectra for the pressed Pt-pellets after different treatments. A Si-spectrum is depicted as reference (black solid line).

Table 5.4: Pt-pellets: Measured lifetimes τ and intensities I as well as mean lifetime τ_m derived from free three-term fits (var = variance of the fit). If not stated otherwise, the measurements were conducted under ambient atmosphere.

	Pt-Pellets			
	τ [ps]	I [%]	τ_m [ps]	*var*
As-prepared	198±4	44.50±2.91	286.5	1.107
	345±5	55.11±2.87		
	2090±260	0.39±0.05		
After oxide reduction	195±6	38.99±3.97	275.8	1.165
	319±5	60.73±3.94		
	2300±340	0.28±0.04		
After tempering at 150 °C	178±5	33.39±2.57	276.4	1.137
	316±3	66.28±2.55		
	2420±290	0.33±0.03		
After tempering at 150 °C (Vacuum)	201±3	48.31±1.48	307.7	1.064
	385±3	51.36±1.47		
	3960±470	0.33±0.02		
After annealing at 500 °C (Vacuum)	165±5	34.48±3.62	253.4	1.112
	265±3	65.25±3.62		
	8600±1700	0.27±0.02		

respective positron lifetime spectrum is marked with red dotted circles in Figure 5.7. The mean lifetime obtained for this state, i.e., $\tau_m = 275.8\,\text{ps}$, also closely fits to the previously obtained values for the dealloyed Pt samples.

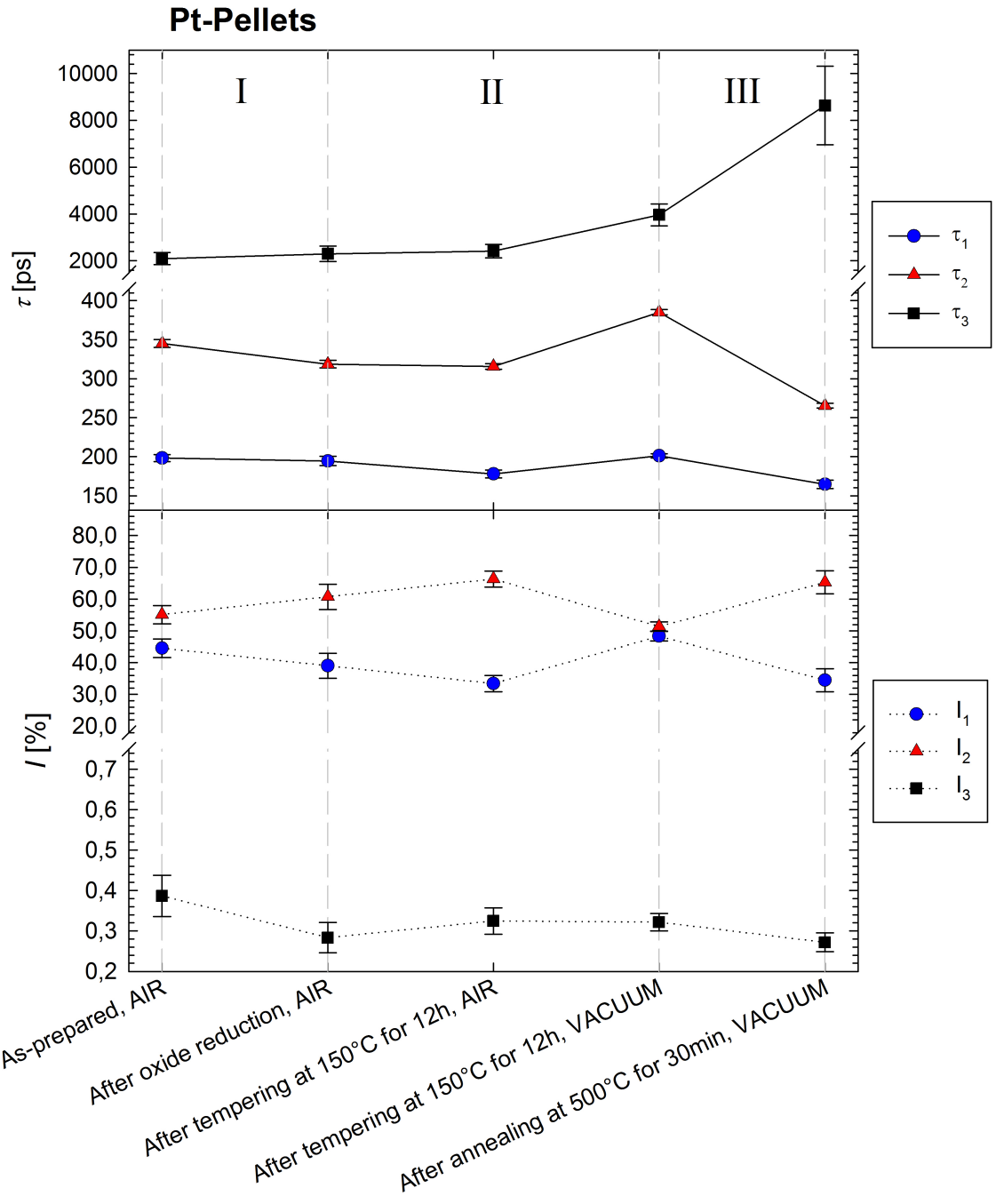

Figure 5.8: Obtained lifetimes and corresponding intensities for different treatments of the Pt-pellets.

After tempering at 150 °C for 12 h

Since the oxide reduction was done electrochemically, electrolyte residues may be caught inside the pores, limiting the positronium formation. With the pellets having the advantage of easily performable heat treatments as compared to the dealloyed samples[9], another tempering step was conducted in order to evaporate potential residues. The experimental details and a pressure/temperature development plot can be found in Section 3.2.6. The observed rise in pressure by less than one order of magnitude cannot be attributed to electrolyte residues, but rather results from evaporation of adsorbed gases from the sample chamber wall.

The lifetime spectrum after tempering is displayed with green triangles in Figure 5.7. Judging from lifetime results, the received lifetime and intensity values of $\tau_2 = 316\,\text{ps}$, $I_2 \approx 66\,\%$ and $\tau_3 = 2.4\,\text{ns}$, $I_3 \approx 0.33\,\%$ closely fit to the values that were derived directly after oxide reduction. Only $\tau_1 = 178\,\text{ps}$ with $I_1 \approx 33\,\%$ is smaller than and not within the error of the corresponding lifetime measured after oxide reduction. However, the constant mean lifetime of 276.4 ps indicates that essentially no changes took place.

After tempering at 150 °C for 12 h, measured in vacuum

The very same samples were now subjected to a lifetime measurement under vacuum condition. The spectrum is marked with yellow triangles in Figure 5.7. The measurement leads to lifetime intensities of $I_1 \approx 48\,\%$ and $I_2 \approx 51\,\%$ while the corresponding lifetimes increase to $\tau_1 = 201\,\text{ps}$ and $\tau_2 = 385\,\text{ps}$, respectively. The long lifetime component rises to 3.9 ns but the intensity remains constant at 0.33 %. As could also be observed for the dealloyed samples, measuring under vacuum conditions increases the mean lifetime, here to 307.7 ps.

After annealing at 500 °C for 30 min, measured in vacuum

As was done for the np-Pt300 samples, the Pt-pellets were annealed at 500 °C as well. The experimental details about this heat treatment can be found in Section 3.2.6. From positron lifetime analysis, three components with a significantly increased lifetime of $\tau_3 = 8.6\,\text{ns}$ and slightly decreased intensity $I_3 = 0.27\,\%$ were derived. The components τ_1 and τ_2 decreased to 165 ps and 265 ps, with intensities of $I_1 \approx 34\,\%$ and $I_2 \approx 66\,\%$. Due to the significantly shortened lifetimes τ_1 and τ_2, the mean lifetime drops by more than 50 ps ($\tau_m = 253.4\,\text{ps}$).

[9] As was described in Section 3.2.6, heat treatments with the dealloyed samples require dissolution of the Crystalbond which leads to very brittle samples.

CHAPTER 6

Discussion

Before going into detail about the positron lifetime results of the different samples, similarities observed for the different stages shall be discussed first. These stages are also labelled by I, II and III in the lifetime/intensity plots in Chapter 5 (Figures 5.4, 5.6 and 5.8). The idea behind this approach is to get a principal idea of what the different measurements reveal about the defects. Since the tempering of the Pt-Pellets yielded the same mean lifetime as directly after oxide reduction, the step 'After tempering at 150 °C for 12 h (vacuum)', shall here synonymously be referred to as 'After oxide reduction (vacuum)' and be described in stage II.

Since a reduced Pt-bulk-lifetime[10] of $\tau < \tau_b = 99\,\text{ps}$ [42] could not be determined, it can be stated that within experimental accuracy, all positrons annihilate in defects and not inside bulk Pt. This can be understood since the positron diffusion length is more than an order of magnitude longer than the ligament size and the crystallite radius, respectively [17]. Therefore, all positrons will eventually get trapped into some kind of defect before annihilating.

[10] The phenomenon of the reduced bulk lifetime was explained in Section 2.3 and can be understood by taking a look at the trapping model. Positrons that get trapped into a defect effectively disappear from the bulk. This disappearance results into a seemingly higher bulk annihilation rate, which in turn reduces the experimentally determined bulk lifetime.

6.1 Conclusions derived from Stages I - III

6.1.1 Stage I: As-prepared → After oxide reduction

- The tendency is the same for the dealloyed (np-Pt180) as well as the compacted sample: The lifetimes τ_1 and τ_2 decrease while the intensity I_2 increases at the cost of I_1. At the same time, τ_3 and I_3 remain constant. While τ_1 decreases only slightly and is constant within the fitting error, the decrease in τ_2 is significant. It is therefore assumed that the change in intensities is a result from the defect attributed to τ_2, while I_1 changes accordingly because of the constant intensity I_3.
  - The fact that τ_2 changes significantly upon oxide reduction points out that τ_2 indicates positron annihilation at oxygen-related surface defects or open volumes and not from closed defects within the ligaments or crystallites, respectively.
  - For the dealloyed sample, the observed effect of τ_2 and I_2 is more pronounced which is in line with cyclic voltammetry measurements. In these measurements, the difference between the first and the last cycle regarding the oxygen desorption region, is much more pronounced for the dealloyed samples as well (see Figures 3.12a and 3.12b).
  - The increase in I_2 suggests that due to the oxygen desorption, either
    * the defect related to τ_2 became more attractive for positron trapping, or
    * that the defect concentration increased, i.e., the surface was restructured, leading to smaller, but more defects. This surface restructuring could be reasonable in the case of the dealloyed samples, since oxygen-atoms are known to have changed places with Pt-atoms during the dealloying process and can be found below the surface in the as-prepared state (PtO ligaments). Furthermore, the decrease in lifetime could also be supportive for a decreasing defect size.

      Regarding the compacted pellets, desorption of the weakly bonded surface oxide will most likely not restructure the surface and I_2 therefore changes only within error.

- The lifetime τ_3 is attributed to o-Ps pick-off annihilation, because it clearly exceeds

the spin-averaged value of 500 ps that was derived as an upper limit for positrons annihilating in metals, irrespective of their annihilation site [39]. We can therefore state that positronium formation seems to be slightly more likely for the dealloyed samples.

  - It then follows that the oxide reduction does not significantly influence the Ps fraction and its lifetime.

- The mean lifetimes in the respective stages are very similar for all samples:
  As-prepared $\tau_m \approx 286$ ps,
  After oxide reduction $\tau_m \approx 275$ ps.

6.1.2 Stage II: After oxide reduction (air) → After oxide reduction (vacuum)

- The tendency in the development of the lifetimes and intensities is the same for all samples when measured in vacuum: All lifetimes increase significantly ($\Delta\tau_1 \approx 20$ ps, $\Delta\tau_2 \approx 40$ to 70 ps) while I_2 decreases at the cost of I_1.

  - The change in lifetimes supports the assumption that the positrons annihilate exclusively from surface defects and open volumes. If defects would exist inside the ligaments or crystallites, respectively, the lifetimes should not change upon measuring under vacuum condition.

    * The shorter lifetimes τ_1 and τ_2 obtained from measurements in air are attributed to the effect of adsorbed gases at surface-defects and open volumes. For instance, an H_2O layer might have formed on the surface, which evaporates upon measuring in vacuum. According to Eldrup et al., the dominant positron lifetime in water at 20 °C is (460 ± 20) ps [43] while Kotera et al. state (400 ± 15) ps [44]. However, these lifetimes are significantly higher than the values obtained for τ_2 after oxide reduction, measured under ambient atmosphere (300 to 315 ps). Furthermore, measuring under vacuum condition should then not increase, but decrease the measured lifetime if positron annihilation also takes place in this H_2O film.

    * The significant increase in the lifetime τ_3 when measured in vacuum can be understood by considering the fact that the o-Ps pick-off lifetime is very sensitive to present gases in free volumes [10].

– The decreasing I_2 could also be indicative for an evaporating H_2O layer, which therefore decreases the number of positrons annihilating with an average τ_2, resulting both from the surface defect and the H_2O layer. However the lifetimes do not support this theory, as was explained above. The decrease in I_2 (increase in I_1) therefore rather indicates that defect type 2 became less attractive (defect type 1 became more attractive) upon measuring in vacuum. This effect is therefore ascribed to the evaporation of adsorbed gases, when measured in vacuum, which alters the trapping potential sensed by the positrons.

6.1.3 Stage III: After oxide reduction (vacuum) → After annealing (vacuum)

- In this stage, the lifetimes and intensities behave differently for the Pt-pellets and the np-Pt prepared by dealloying. However, the fact that the short lifetime component is still present after annealing also confirms that this defect cannot be attributed to vacancies inside the grains and ligaments, respectively. According to vacancy annealing experiments in Pt after electron irradiation, vacancies become mobile at temperatures of 227 °C or higher (Stage III [45]). This result is in line with the observed rise in lifetime when comparing measurements under atmosphere with those in vacuum.

6.2 Detailed Positron Lifetime Analysis

Since the defect and surface/interface physics is better understood for the compacted pellets, the lifetime data for these samples shall be discussed first and serve somehow as a reference for the dealloyed samples.

6.2.1 Pt-Pellets

The measured lifetimes τ_1 between 165 ps and 201 ps are longer than the lifetime of 99 ps [42] observed for defect-free Pt. Therefore, these lifetimes can be attributed to annihilation events at the interface between two adjacent crystallites, as was previously also described for compacted Fe pellets by Schaefer et al. [46]. Due to the different crystallite orientations at such an interface, vacancy-like defects of the size of approximately a monovacancy can be expected. For Pt, Schaefer et. al reported $\tau_{1v} = (168 \pm 3)$ ps and $\tau_{2v} = (174 \pm 3)$ ps as lifetimes for single- and divacancies, respectively [42], while Brauer et al. stated $\tau_{1v} = (174 \pm 3)$ ps and $\tau_{2v} = (206 \pm 3)$ ps [47]. The measured lifetime τ_1 can therefore be well

explained by vacancy-like defects at the interfaces between two adjacent crystallites.
This result for τ_1 is further evidenced by the fact that a short component of (165 ± 5) ps is still present after annealing at T = 500 °C for 30 min, where monovacancies inside the crystallites would have annealed out already [45].
Furthermore, since the lifetime τ_1 increases significantly when measured in vacuum, this defect cannot be located inside the crystallites, but must rather be located at an interface.

The lifetime τ_2 can be explained by sub-nanometer micro-voids that develop where more than two crystallites join and form an open volume. Lifetimes in such open volumes have been measured for nanocrystalline Fe-pellets (crystallite radius ≈ 6 nm) and reported to be $\tau = (360 \pm 30)$ ps [46]. Also in nanocrystalline gold with crystallite radii ranging from 7 to 15 nm, a component with 370 ps was found and attributed to such micro-voids [48]. These measurements were conducted under vacuum and the results fit nicely to the lifetime of (385 ± 3) ps, obtained for the Pt-pellets in vacuum (crystallites of 5 to 7 nm in diameter).
A significant 70 ps increase of τ_2 when measured under vacuum condition is also strongly supportive for the interpretation of open volume micro-voids, since the lifetime for a defect inside a crystallite should not change whether or not the measurement is conducted in vacuum.

Finally, the long-lived annihilation event with τ_3 between about 2 and 8 ns is attributed to pick-off annihilation of o-Ps inside larger voids. Long lifetimes between 1 and 4 ns have also been reported for nanocrystalline Fe pellets with intensities of $I_3 + I_4$ as high as 30 % (depending on the annealing temperature) [46]. However, the fact that in the present experiments intensities are only approximately 0.3 % is rather surprising. It may be partially explained by a decay of the intrinsic pick-up probability as the positron work function becomes more negative (Nieminen et al. [2]). The positron work functions for polycrystalline surfaces of Pt and Fe are $\Phi_{+,Pt} = (-1.8 \pm 0.2)$ eV and $\Phi_{+,Fe} = (-1.2 \pm 0.2)$ eV, respectively [11].

Another interesting feature is observed after the annealing step at $T = 500$ °C. Both lifetimes decrease which can be ascribed to free volume shrinkage. In fact, a macroscopical shrinkage could be observed and the estimated porosities of the two pellets decreased from about 75 % to approximately 40 % during the annealing step. This corresponds to a decrease of the specific surface area from approximately 17 $\mathrm{m^2/g}$ to 1 $\mathrm{m^2/g}$. Furthermore, the intensity I_1 decreases which indicates a decrease in the interfacial area due to grain growth.

6.2.2 np-Pt

The lifetime τ_1 with 169 to 193 ps suggests vacancy-like defects existing in the nanoporous samples. While Viswanath et. al found evidence for vacancies in np-Au ligaments and observed a continuous decrease in τ_1 down to the bulk value upon annealing [13], this phenomenon is not observed in the present study for np-Pt. The fact that this short component also exists after annealing at 500 °C points either to a stabilizing effect of the vacancies by impurities (Cu), or to a structural surface defect. However, the charge amount obtained by electrochemical means during dealloying suggests that the copper residues inside the np-Pt300 samples are negligible ($\approx$ 100 % Cu dissolution). The observed high value of approximately 53 % for this lifetime component after annealing therefore cannot be attributed to a vacancy stabilizing effect by impurity-vacancy complexes. Furthermore, as was discussed before, the lifetime change upon measuring in vacuum already showed that this defect species cannot be located inside the ligaments.

The lifetime τ_2 with values ranging from 302 to 394 ps must also correspond to a surface defect as vacuum measurements showed. In as-dealloyed np-Au, Viswanath et al. found a lifetime of $\approx$ 440 ps with 50 % intensity and ascribed it to positrons annihilating from large vacancy clusters or voids at the ligament/pore interface, i.e., at the surface [13]. Because of the small, sub-nm size of such surface defects, verifying their existence might be difficult.
Another possible explanation for this lifetime could be the trapping of positrons at the surface potential well. According to Nieminen et. al [2], the lifetime in such a surface state should be close to the spin-averaged lifetime, i.e., about 500 ps, which was derived under the assumption that each positron is screened by one electron [39]. If we assume that for metals with highly negative positron work functions (such as Pt), a positron inside the surface state might be screened by more than one electron because of the stronger dipole layer, the positron lifetime could be shortened further and better fit to the observed lifetimes. If τ_2 really corresponds to positrons annihilating from surface states, an in-situ measurement of positron lifetime spectra during heating should result in an increase of I_3 at the cost of I_2 because of the thermally activated detrapping of the positrons as Ps (compare (2.11)). However, heating nanoporous samples would also result in coarsening of the structure and change the surface condition, which makes this experiment less attractive.

The lifetime τ_3 can clearly be attributed to quenched o-Ps annihilation inside the pores, as was discussed earlier for the Pt-pellet samples.
Contrary to the results obtained for np-Au by Viswanath et al. [13], heat-treating the np-Pt

samples does not significantly influence the Ps formation.

CHAPTER 7

Conclusion

In this work, nanoporous Pt samples with a high specific surface area were prepared by means of electrochemical dealloying of $Cu_{75}Pt_{25}$ ($\approx 40\,{}^{m^2}/_{g}$) and by powder compaction ($\approx 17\,{}^{m^2}/_{g}$). Subsequently, the fabricated samples were investigated with the method of positron annihilation lifetime spectroscopy. The aim of this work was to investigate the formation probability and behavior of the lifetime of o-Ps, which was assumed to form with substantial intensity inside the free volume of the fabricated samples due to the negative positron work function of Pt.

In fact, such a long-lived annihilation event was found in all positron lifetime spectra measured after different sample treatments. The component with a lifetime of approximately 2 ns is attributed to o-Ps pick-off annihilation in the interconnected pores (np-Pt) and bigger voids (Pt-pellets) and shows an increase by up to 2.5 ns when measured in vacuum. This significant change is attributed to the evaporation of adsorbed gases on the pore wall that quench the o-Ps lifetime during collisions with the latter. However, the most outstanding result from the measurements conducted is that the Ps formation seems very unlikely in both the dealloyed as well as the compacted Pt samples. In fact, the fraction of Ps formed is smaller than 0.6 % in all measurements, irrespective of the conducted sample treatments and measuring conditions.

We also learn from positron lifetime measurements that no positrons annihilate in the bulk material (ligaments for np-Pt and crystallites for compacted pellets) but all get trapped into some kind of defect. A comparison of sample-specific lifetimes derived from measurements conducted under ambient atmosphere with measurements done in vacuum shows an increase

in all lifetimes. This indicates that all defects must be either surface defects (τ_1, τ_2), or correspond to a free, interconnected volume consisting of pores and voids (τ_3). Depending on the sample treatment and measuring condition, the first two lifetimes were derived as $\tau_1 = (180 \pm 15)\,\mathrm{ps}$ and $\tau_2 = (350 \pm 50)\,\mathrm{ps}$, and attributed to vacancy-sized defects and micro-voids, respectively.

Bibliography

[1] B. Y. Tong. Negative Work Function of Thermal Positrons in Metals. *Phys. Rev. B* **5** (1972) 1436.
DOI: 10.1103/PhysRevB.5.1436

[2] R. M. Nieminen, J. Oliva. Theory of positronium formation and positron emission at metal surfaces. *Phys. Rev. B* **22** (1980) 2226.
DOI: 10.1103/PhysRevB.22.2226

[3] K. F. Canter, A. P. Mills, S. Berko. Efficient Positronium Formation by Slow Positrons Incident on Solid Targets. *Phys. Rev. Lett.* **33** (1974) 7.
DOI: 10.1103/PhysRevLett.33.7

[4] A. P. Mills. Positronium Formation at Surfaces. *Phys. Rev. Lett.* **41** (1978) 1828.
DOI: 10.1103/PhysRevLett.41.1828

[5] A. P. Mills, P. M. Platzman, B. L. Brown. Slow-Positron Emission from Metal Surfaces. *Phys. Rev. Lett.* **41** (1978) 1076.
DOI: 10.1103/PhysRevLett.41.1076

[6] A. P. Mills. Thermal activation measurement of positron binding energies at surfaces. *Solid State Communications* **31** (1979) 623.
DOI: 10.1016/0038-1098(79)90310-7

[7] K. Lynn, P. Schultz, I. MacKenzie. Low-temperature measurements of the fraction of re-emitted positronium from a Cu(111)+S surface. *Solid State Communications* **38** (1981) 473.
DOI: 10.1016/0038-1098(81)90419-1

[8] R. H. Howell, I. J. Rosenberg, M. J. Fluss. Production of energetic positronium at metal surfaces. *Phys. Rev. B* **34** (1986) 3069.
DOI: 10.1103/PhysRevB.34.3069

[9] G. Schatz, A. Weidinger, M. Deicher. *Nukleare Festkörperphysik.* Springer Vieweg, 2010

[10] D. W. Gidley, H.-G. Peng, R. S. Vallery. POSITRON ANNIHILATION AS A METHOD TO CHARACTERIZE POROUS MATERIALS. *Annual Review of Materials Research* **36** (2006) 49.
DOI: 10.1146/annurev.matsci.36.111904.135144

[11] M. Jibaly, A. Weiss, A. R. Koymen, D. Mehl, L. Stiborek, C. Lei. Measurement of the positron work functions of polycrystalline Fe, Mo, Ni, Pt, Ti, and V. *Phys. Rev. B* **44** (1991) 12166.
DOI: 10.1103/PhysRevB.44.12166

[12] D. V. Pugh. *Nanoporous Platinum.* Dissertation, Virginia Polytechnic Institute and State University, 2003

[13] R. N. Viswanath, V. A. Chirayath, R. Rajaraman, G. Amarendra, C. S. Sundar. Ligament coarsening in nanoporous gold: Insights from positron annihilation study. *Applied Physics Letters* **102** (2013) 253101.
DOI: 10.1063/1.4812290

[14] R. Krause-Rehberg, H. Leipner. *Positron Annihilation in Semiconductors.* Springer-Verlag, 1999

[15] A. Perkins, J. P. Carbotte. Effect of the Positron-Phonon Interaction on Positron Motion. *Phys. Rev. B* **1** (1970) 101.
DOI: 10.1103/PhysRevB.1.101

[16] J. Oliva. Inelastic positron scattering in an electron gas. *Phys. Rev. B* **21** (1980) 4909.
DOI: 10.1103/PhysRevB.21.4909

[17] C. Szeles, K. G. Lynn. Positron-Annihilation Spectroscopy. *Encyclopedia of Applied Physics*, Band 13/14 (Herausgeber G. L. Trigg). WILEY-VCH, 2004

[18] W. Brandt, R. Paulin. Positron implantation-profile effects in solids. *Phys. Rev. B* **15** (1977).
DOI: 10.1103/PhysRevB.15.2511

[19] M. J. Puska, R. M. Nieminen. Theory of positrons in solids and on solid surfaces. *Rev. Mod. Phys.* **66** (1994) 841.
DOI: 10.1103/RevModPhys.66.841

[20] P. Hautojärvi (Herausgeber). *Positrons in Solids.* Springer Verlag Berlin Heidelberg New York, 1979

[21] A. Bisi, L. Bosi, E. Lazzarini, L. Zappa. Positronium spin conversion in Li-ammonia solution. *The Journal of Chemical Physics* **63** (1975) 5087.
DOI: 10.1063/1.431315

[22] R. Nieminen, C. Hodges. Positron work functions in transition metals. *Solid State Communications* **18** (1976) 1115.
DOI: 10.1016/0038-1098(76)91254-0

[23] D. G. Costello, D. E. Groce, D. F. Herring, J. W. McGowan. Evidence for the Negative Work Function Associated with Positrons in Gold. *Phys. Rev. B* **5** (1972) 1433.
DOI: 10.1103/PhysRevB.5.1433

[24] C. H. Hodges, M. J. Stott. Work Functions for Positrons in Metals. *Phys. Rev. B* **7** (1973) 73.
DOI: 10.1103/PhysRevB.7.73

[25] E. M. Gullikson, A. P. Mills, C. A. Murray. Dependence of the positron reemission probability on the positron work function of a metal surface. *Phys. Rev. B* **38** (1988) 1705.
DOI: 10.1103/PhysRevB.38.1705

[26] P. Kirkegaard, J. V. Olsen, M. Eldrup, N. J. Pedersen. *PALSfit: A computer program for analysing positron lifetime spectra.* RisøDTU, 2009

[27] J. Erlebacher, M. J. Aziz, A. Karma, N. Dimitrov, K. Sieradzki. Evolution of nanoporosity in dealloying. *NATURE* **410** (2001).
DOI: 10.1038/35068529

[28] A. Kloke, F. von Stetten, R. Zengerle, S. Kerzenmacher. Strategies for the Fabrication of Porous Platinum Electrodes. *Adv. Mater.* **23** (2011) 4976.
DOI: 10.1002/adma.201102182

[29] D. V. Pugh, A. Dursun, S. G. Corcoran. Formation of nanoporous platinum by selective dissolution of Cu from Cu0.75Pt0.25. *Journal of Materials Research* **18** (2003) 216.
DOI: 10.1557/JMR.2003.0030

[30] J. Erlebacher, R. C. Newman, K. Sieradzki. Fundamental Physics and Chemistry of Nanoporosity Evolution During Dealloying. *Nanoporous Gold From an Ancient Technology to a High-Tech Material* (Herausgeber A. Wittstock, J. Biener, J. Erlebacher, M. Bäumer). RSC Publishing, 2012

[31] K. Sieradzki, N. Dimitrov, D. Movrin, C. McCall, N. Vasiljevic, J. Erlebacher. The Dealloying Critical Potential. *Journal of the Electrochemical Society* **149** (2002) B370.
DOI: 10.1149/1.1492288

[32] H.-J. Qiu, L. Peng, X. Li, H. Xu, Y. Wang. Using corrosion to fabricate various nanoporous metal structures. *Corrosion Science* **92** (2015) 16.
DOI: 10.1016/j.corsci.2014.12.017

[33] D. V. Pugh, A. Dursun, S. G. Corcoran. Electrochemical and Morphological Characterization of Pt-Cu Dealloying. *Journal of the Electrochemical Society* **152** (2005) B455.
DOI: 10.1149/1.2048140

[34] M. Besenhard. *Synthesis and Tunable Properties of Nanoporous Platinum.* Diplomarbeit, Graz University of Technology, 2010

[35] S. Trasatti, O. Petrii. Real surface area measurements in electrochemistry. *Journal of Electroanalytical Chemistry* **327** (1992) 353.
DOI: 10.1016/0022-0728(92)80162-W

[36] B. Predel. Cu-Pt (Copper-Platinum). Springer-Verlag GmbH, Heidelberg, 1994.
DOI: 10.1007/10086090_1106

[37] J. Erlebacher. An Atomistic Description of Dealloying: Porosity Evolution, the Critical Potential, and Rate-Limiting Behavior. *Journal of The Electrochemical Society* **151** (2004) C614.
DOI: 10.1149/1.1784820

[38] H. Angerstein-Kozlowska, B. Conway, W. Sharp. The real condition of electrochemically oxidized platinum surfaces: Part I. Resolution of component processes. *Journal of Electroanalytical Chemistry and Interfacial Electrochemistry* **43** (1973) 9.
DOI: 10.1016/S0022-0728(73)80307-9

[39] A. Seeger, F. Banhart. On the Systematics of Positron Lifetimes in Metals. *physica status solidi (a)* **102** (1987) 171.
DOI: 10.1002/pssa.2211020117

[40] P. Mascher, S. Dannefaer, D. Kerr. Positron trapping rates and their temperature dependencies in electron-irradiated silicon. *Phys. Rev. B* **40** (1989) 11764.
DOI: 10.1103/PhysRevB.40.11764

[41] P. Kindl, W. Puff, H. Sormann. A free four-term analysis of positron lifetime spectra of γ-irradiated Teflon. *physica status solidi (a)* **58** (1980) 489.
DOI: 10.1002/pssa.2210580219

[42] H. Schaefer, W. Stuck, F. Banhart, W. Bauer. Thermal vacancies in the noble metals Cu, Ag, Au, and in Pt studied by positron lifetime spectroscopy. *Materials Science Forum*, Band 15-18, 1987 S. 117–24.
DOI: 10.4028/www.scientific.net/MSF.15-18.117

[43] M. Eldrup, O. Mogensen, G. Trumpy. Positron Lifetimes in Pure and Doped Ice and in Water. *The Journal of Chemical Physics* **57** (1972) 495.
DOI: 10.1063/1.1677990

[44] K. Kotera, T. Saito, T. Yamanaka. Measurement of positron lifetime to probe the mixed molecular states of liquid water. *Physics Letters A* **345** (2005) 184.
DOI: 10.1016/j.physleta.2005.07.018

[45] P. Ehrhart. *Atomic Defects in Metals* (Herausgeber H. Ullmaier). Springer-Verlag GmbH, Heidelberg, 1991.
DOI: 10.1007/10011948_66

[46] H. Schaefer, R. Würschum. Positron lifetime spectroscopy in nanocrystalline iron. *Physics Letters A* **119** (1987) 370.
DOI: 10.1016/0375-9601(87)90618-9

[47] G. Brauer, W. Anwand, E.-M. Nicht, J. Kuriplach, I. Procházka, F. Bečvář, A. Osipowicz, P. G. Coleman. Characterization of rf-sputtered platinum films by positron annihilation spectroscopy. *Phys. Rev. B* **62** (2000) 5199.
DOI: 10.1103/PhysRevB.62.5199

[48] Y. Ito, S. Takamura, M. Kobiyama. Nano-Crystalline Gold Studied by Positron Annihilation. *physica status solidi (a)* **179** (2000) 297.
DOI: 10.1002/1521-396X(200006)179:2<297::AID-PSSA297>3.0.CO;2-Y

APPENDIX A

Appendix

Programs for Data Pre-processing

Since the spectrometer is rather sensitive to external influences, e.g., temperature or voltage fluctuations, it is advisable to record many short time spectra instead of just one long spectrum. This way, spectra that experienced a time shift and would have broadened the spectrum if recorded cumulatively, can be rejected. The satisfactory spectra are then summed up to a single spectrum which can later be used for numerical analysis with the program PALS*fit*.
The recording of the single spectra was initialized with the program `START_Messung` that requires the number of the first spectrum, the number of spectra to be recorded and the recording time for each spectrum. The single spectra will then be named SDxxxx.TKA where xxxx stands for the respective spectrum number.

For the purpose of pre-processing of these collected single spectra, several programs were written in C and shall be explained briefly.

`1_TRANSAPT_ff.exe`

This program reads multiple recorded lifetime spectra and writes the data into one output-file with the extension *.dat*. The single spectra are listed in a column and are separated by eleven dashes. A filename with up to 25 characters can be chosen for the newly generated file.

Input:

- Repeating spectrum name without enumeration
- Number of the first spectrum
- Number of the last spectrum
- Desired name of generated file

`2_MOMENT.exe`

This program calculates the first momentum of each single spectrum, i.e., the channel where the number of counts is equal to the right and to the left. Since in most cases the fist momentum will not be in the middle of a channel, the counts within this channel are distributed in order to get the exact position of the first momentum (given with five digits accuracy). A file with the extension *.mom* and the name of the input-file will be generated, containing the first momenta of each spectrum. From these first momenta it can subsequently be decided which of the spectra should be further processed.

Input:

- Name of file containing the single spectra (including the extension *.dat*)

`3_SUMMEN.exe`

With this program, all satisfying spectra can be summed up channel-wise and are stored as a column vector. A file with the extension *.sum* and the name of the input-file will be generated. This routine works in two modi: 1) All spectra are chosen. 2) A number of ranges of spectra is chosen. In the first line of the output-file, the ranges will be printed. Furthermore, to avoid problems with logarithmic plots, all channels that exhibit zero counts after the summation are set to the value one by the program.

Input:

- Name of file containing the single spectra (including the extension *.dat*)
- Spectrum selection mode
  - Mode 1: No further input is required

– Mode 2: The number of ranges and the respective beginning and ending have to be declared

`4_SPEKTRAN.exe`

This program transforms the vector of the sum-spectrum into an array of 10 right aligned integers in each line, because this is the preferred reading format for PALS*fit*. Furthermore, the program displays the number of channels in the spectrum. If wished, parts of the background tail to the right of the spectrum can be truncated. The output-file will have the extension *.po* and is named like the input-file. PALS*fit* interprets the first line as header, which is why this line contains the filename.

Input:

- Name of file containing the summed spectrum (including the extension *.sum*)
- Number of channels that will be processed (counted from the beginning)

`5_SPEKPLOT.exe`

With `SPEKPLOT`, a peak-normalized spectrum can be generated from the sum-spectrum. This is particularly useful if many spectra are plotted together since differences in the slopes of the spectra can be seen more easily. The generated output-file has a *.plo* extension and the name of the input-file.

Input:

- Name of file containing the summed spectrum (including the extension *.sum*)

Acknowledgment

I would like to thank several people for their support during this work:

Univ.-Prof. Dr. Roland Würschum, Institute of Materials Physics, TU Graz
For making the work on this stimulating research idea possible at the institute and for the helpful advice in positron lifetime data interpretation.

Assoc.Prof. Dr. Wolfgang Sprengel, Institute of Materials Physics, TU Graz
For the supervision and the valuable input during the writing process of this work, and most importantly for his humorous way of teaching.

Dipl.-Ing. Stefan Topolovec, Institute of Materials Physics, TU Graz
For his constructive and useful ideas about sample fabrication and for answering every question about electrochemistry.

Dipl.-Ing. Gregor Klinser, Institute of Materials Physics, TU Graz
For helping with the calibration of the spectrometer and for numerous valuable discussions about positron physics.

Dipl.-Ing. Dr. Martin Luckabauer, Institute of Materials Physics, TU Graz
For providing me with useful tips about C programming.

The group of Prof. Dr.-Ing Weißmüller, Institute of Materials Research, Helmholtz-Zentrum Geesthacht
For kindly providing the $Cu_{75}Pt_{25}$ alloys.